Turbulence Characteristics and Dissipation Estimates in the Coastal Ocean Bottom Boundary Layer from PIV Data

P. DORON, L. BERTUCCIOLI, AND J. KATZ

Department of Mechanical Engineering, The Johns Hopkins University, Baltimore, Maryland

T. R. OSBORN

Department of Mechanical Engineering and Department of Earth and Planetary Sciences, The Johns Hopkins University, Baltimore, Maryland

(Manuscript received 23 April 1999, in final form 4 October 2000)

ABSTRACT

Turbulence characteristics in the coastal ocean bottom boundary layer are measured using a submersible Particle Image Velocimetry (PIV) system with a sample area of 20×20 cm^2. Measurements are performed in the New York Bight at elevations ranging from 10 cm to about 1.4 m above the seafloor. Recorded data for each elevation consists of 130 s of image pairs recorded at 1 Hz. After processing, the data at each elevation consist of 130 instantaneous spatial velocity distributions within the sample area. The vertical distribution of mean velocity indicates the presence of large-scale shear even at the highest measurement station. The flow also undergoes variations at timescales longer than the present data series.

Spatial spectra of the energy and dissipation are calculated from individual vector maps. The data extend well beyond the peak in the dissipation spectrum and demonstrate that the turbulence is clearly anisotropic even in the dissipation range. The vector maps are also patched together to generate extended velocity distributions using the Taylor hypothesis. Spectra calculated from the extended data cover about three decades in wavenumber space. For the overlapping range the extended spectra show small differences from those determined using the instantaneous distributions. Use of the Taylor hypothesis causes ''contamination'' of the extended spectra with surface waves. Nevetheless, the results still indicate that the turbulence is also anisotropic at low wavenumbers (energy containing eddies). The vertical component of velocity fluctuations at energy containing scales is significantly damped as the bottom is approached, while the horizontal component maintains a similar energy level at all elevations.

Different methods of estimating the turbulent energy dissipation are compared. Several of these methods are possible only with 2D data, such as that provided by PIV, including a ''direct'' method, which is based on measured components of the deformation tensor. Estimates based on assumptions of isotropy are typically larger than those based on the direct method (using available velocity gradients and least number of assumptions), but the differences vary from 30% to 100%.

1. Introduction

In the coastal ocean the momentum and energy balances are influenced by several parameters, among which the bottom shear stress and the dissipation rate are of particular significance. The bottom shear stress affects the circulation directly and also generates turbulence that diffuses into the flow. The dissipation rate is a controlling mechanism for the entire turbulent energy budget. Thus, understanding and modeling of ocean flows, sediment transport, pollutant dispersal, and biological processes rely on knowledge of the turbulence characteristics near the ocean bottom.

Corresponding author address: Dr. Joseph Katz, Dept. of Mechanical Engineering, The Johns Hopkins University, 200 Latrobe Hall, 3400 N. Charles St., Baltimore, MD 21218.
E-mail: katz@titan.me.jhu.edu

Several means to measure the turbulence and flow characteristics near the ocean floor have been developed: some involving direct measurements, and others relying on an assumed velocity profile or turbulence characteristics. For example, a least squares fit to a measured mean velocity profile can be used to estimate the friction velocity and the bottom roughness length scale, assuming that a logarithmic, constant stress layer exists. This method is sensitive to errors in the height of the sensors (Grant et al. 1984) and in zero offset (Huntley and Hazen 1988). It also requires several velocity sensors with good calibration and stability.

Assuming a balance between turbulent kinetic energy production and dissipation, one can estimate the dissipation from a fit of the Kolmogorov $-5/3$ spectral slope in the inertial range of the vertical velocity spectrum. Using the dissipation and a measured velocity shear,

one can then solve for the bottom stress (Grant et al. 1984; Johnson et al. 1994). These approaches depend on the validity of the production–dissipation balance, on estimating spatial spectral levels from temporal spectra, and on the accuracy of estimates of dissipation from the $-5/3$ spectral slope. Alternatively, if data is available at sufficiently small scales, one may estimate the dissipation from a fit of the universal spectrum in the dissipation range (Dewey and Crawford 1988). This method still relies on assumed isotropy.

Turbulent stress measurements can be performed using acoustic methods. Acoustic Doppler current profilers (ADCPs) are the most popular and have been used extensively. For example, Lohrmann et al. (1990) and Lu and Lueck (1999) use four-beam instruments to measure three velocity components. Lhermitte and Lemmin (1994) measure two velocity components with a three-beam ADCP and fit velocity profiles with logarithmic curves to estimate the shear stress. This technique assumes horizontal homogeneity of the horizontal velocity and the second-order moments of the turbulent velocities. Estimates of Reynolds stresses are susceptible to contamination by tilt of the instrument in anisotropic turbulence. Van Haren et al. (1994) use the variance technique on ADCP data to estimate the Reynolds stress, and combine vertical velocity fluctuation measurements with temperature data to estimate the buoyancy flux. They measure the momentum flux, estimate the eddy viscosity, and form an approximate energy balance. Lu and Lueck (1999) discuss the errors and uncertainties of ADCP measurements of turbulence using the variance technique. The Doppler shift of acoustic signal reflection is also employed in the Acoustic Doppler Velocimeter (ADV) for point measurements of 3D velocity components (Kraus et al. 1994; George 1996; Voulgaris and Trowbridge 1998).

The Benthic Acoustic Stress Sensor system, which is based on acoustic travel time measurements, has been developed to measure the velocity from bottom-mounted tripods (Williams et al. 1987; Gross et al. 1994; Williams et al. 1996). Fitting logarithmic profiles to data collected at different elevations can yield estimates of stress (e.g., Johnson et al. 1994; Trowbridge and Agrawal 1995; Trowbridge et al. 1996). The finite sensor volume of this instrument affects the spatial resolution of the measurement.

Sanford et al. (1999) utilize an advanced electromagnetic velocity and vorticity sensor for measuring finescale fluctuations. Sanford and Lien (1999) use this instrument to measure downstream and vertical velocity components as well as fluctuations in a tidal channel, from which Reynolds stress is calculated in 1-m vertical bins. The spatial response of this sensor could suffice for resolving the turbulence structure a few meters above the boundary, but very near the bottom the stress would likely be underestimated. An electromagnetic current meter is also used by Winkel et al. (1996) to provide a reference for acoustic current meter readings.

Laser Doppler Velocimetry (LDV) has been used extensively for measurements of turbulence in laboratories. Oceanic field applications have been infrequent, the primary contributions originating from Agrawal and colleagues (Agrawal and Aubrey 1992; Trowbridge and Agrawal 1995; Agrawal 1996). This point measurement technique can have excellent spatial resolution, but to achieve a small sample volume, one needs to perform the measurements close to the probe. Measurements at longer distances require complex optics or compromises in sample volume size. The LDV data quality also depends on the water transmissivity and on the size of the particles crossing the sample volume.

In a previous paper (Bertuccioli et al. 1999), we have introduced the application of particle image velocimetry (PIV) to oceanic measurements. Unlike all other techniques, PIV provides the instantaneous distribution of two velocity components over a sample area. Combination of PIV with stereo photography that has become quite popular in laboratory experiments can be used for measuring all three velocity components in the sample area. Consequently, PIV enables measurements of spatial spectra without assumption involving Taylor's hypothesis or homogeneity (Liu et al. 1994). PIV has already been implemented in a variety of forms (e.g., Adrian 1991; Grant 1997), but in most laboratory applications the fluid is seeded with microscopic tracer particles, and a selected sample area is illuminated with a laser light sheet. We have found that in the ocean natural seeding is sufficient for obtaining high quality PIV data. To obtain a single dataset (i.e., one realization of the spatial velocity distribution within the sample area) the light sheet is pulsed twice, and the particle images are recorded on a single frame or on separate frames. During typical analysis, the images are divided into small subwindows and peaks of the correlation function of the intensity distribution yield the mean displacement of all the particles within each window. A sequence of PIV data provides a time series of the spatial distribution in the sample area. Such data can produce information on the entire flow structure, such as velocity profiles, turbulence intensity and shear stress, vorticity distributions, and dissipation and turbulent spectra.

In the present paper we present data acquired with the submersible PIV system in the bottom boundary layer off Sandy Hook, New Jersey, in June 1998. We first describe the instrument and the analysis procedures in section 2. Basic characterization of the flow is presented in section 3. Velocity spectra are presented in section 4, followed by a discussion of turbulent kinetic energy dissipation in section 5. The effects of interpolating velocity distributions and of the interaction of surface waves and turbulence are examined in sections 6 and 7.

2. Instrumentation and analysis procedures

a. Apparatus

A detailed description of the oceanic PIV system can be found in Bertuccioli et al. (1999), and only a brief

summary is provided here for completeness. A schematic overview of the surface-mounted light source, data acquisition, and control subsystems is shown in Fig. 1a, and the submersible PIV system is shown in Fig. 1b. The light source is a dual-head, pulsed dye laser, which provides 2-μs pulses of light at 594 nm, with energy of up to 350 mJ/pulse. The light is delivered through an optical fiber to a submerged optical probe, where the beam is expanded to a sheet that illuminates the sample area. Based on tests in the lab the maximum energy output at the end of the fiber is 120 mJ/pulse. Images are acquired using a 1024 $\times$ 1024 pixel (1008 $\times$ 1018 active pixels) Kodak Megaplus-XHF CCD camera, which can acquire up to 15 pairs of frames per second, with essentially unlimited in-pair delay.

The submersible system also contains a Sea-Bird Electronics SeaCat 19-03 CTD, optical transmission and dissolved oxygen content sensors, a ParoScientific Digiquartz Model 6100A precision pressure transducer, an Applied Geomechanics Model 900 biaxial clinometer, and a KVH C100 digital compass. The platform is mounted on a hydraulic scissor-jack to enable acquisition of data at various elevations above the seafloor (the current maximum range is 1.8 m). The platform can also be rotated to align the sample area with the mean flow direction. The flow direction is found by monitoring the orientation of a vane mounted on the platform with a submersible video camera.

b. Data acquisition and analysis

As noted before, PIV involves illumination of a sample plane with a light sheet and recording of multiple images of the particles within this area. Typically the image is divided into small windows and correlation analysis is used to determine the mean displacement within each window. To obtain a high signal-to-noise ratio we have opted to acquire pairs of images (each exposure on a separate frame) and use cross-correlation for analysis (Keane and Adrian 1992). Details of the image analysis procedures can be found in Dong et al. (1992), Roth et al. (1995, 1999), Sridhar and Katz (1995), and Bertuccioli et al. (1999). Laboratory studies have shown that an absolute subpixel accuracy of about 0.4 pixels can be obtained using a conservative estimate equal to twice the standard deviation between exact and measured displacements. Such a level can be achieved when there is a sufficient number of particles per window (5–10), and other requirements involving particle image size and local velocity gradients are also satisfied. This uncertainty corresponds to a relative accuracy of better than 2% if the typical displacement is more than 20 pixels.

With a nominal image size of 1024 $\times$ 1024 pixels (active size 1008 $\times$ 1018 pixels), an interrogation window size of 64 $\times$ 64 pixels and 50% overlap between adjacent windows, each image pair produces a velocity map of 29 $\times$ 29 vectors. The magnification is measured directly during each deployment at the test site. For the tests reported here, the measured magnification is 50.9 pixels/cm, yielding a field of view of 20.1 cm $\times$ 20.1 cm. Each interrogation window then covers an area of 12.6 mm $\times$ 12.6 mm, with a spacing of 6.3 mm between vectors (Fig. 3). Our first generation of the data acquisition systems enables acquisition of 130 image pairs, that is, a data series of a little more than two minutes long. As discussed in section 5a, for some of the analysis we combine this data series to obtain spectra at scales larger than the image size. A recently acquired massive data acquisition system that is replacing the current setup has a storage capacity of 240 GB.

c. Deployment

The submersible PIV system was deployed in the New York Bight near the Mud Dump Site, 7 miles east of Sandy Hook, New Jersey, in June 1998 (Fig. 2). The data was taken at station EPA05 (40.42°N, 73.86°W), within the Expanded Mud Dump area. This region was used until 1977 for dumping dredged material brought from New York by barges, and was later covered with sand to prevent dispersal of pollutants. The station is close to the summit of an approximately 6 km $\times$ 3 km elevated area, whose long axis is in the north–south direction. The depth near the summit is about 15 m, with the surrounding area being about 25 m deep. The bottom slope at the test site is approximately 3 m km^{-1} (SAIC 1995; Schwab et al. 1997).

The bottom composition surveyed in October 1995, is mostly sandy with no mud or silt. The grain size is ϕ 1–3 (0.125–0.5 mm), with a major mode of ϕ 1–2 (SAIC 1995). Since no dredged material was added to the site since the date of the survey, we assume that this data is still adequate. The sandy environment is favorable for PIV measurements, since the coarse sand settles quickly, leaving relatively clear water. Visibility measurements done during the experiment indicate light transmission of more than 80% (measured with the SeaCat, 25-cm pathlength transmissometer). Note that in another deployment, off Cape May, New Jersey, we acquired data successfully also when the transmission was less than 50%.

The instrument was submerged from the deck of the R/V *Walford*, set on a three-point anchor (with the anchors laid 50–100 m from the boat). After it hit the bottom, the platform was raised to the topmost elevation and rotated until the vane indicated proper alignment with the mean flow. The same platform orientation was maintained for the entire experiment at all elevations. Series of 130 image pairs were obtained at six different elevations (z), with the sample areas centered at z = 20 (i.e., 10–30 cm from the floor), 44, 62, 82, 106, and 128 cm above the bottom. This data spans elevations from 10 cm up to 138 cm above the bottom, covering the range of 0.9–1.3 m reported by Huntley (1988) for the thickness of the bottom log layer. Data was first

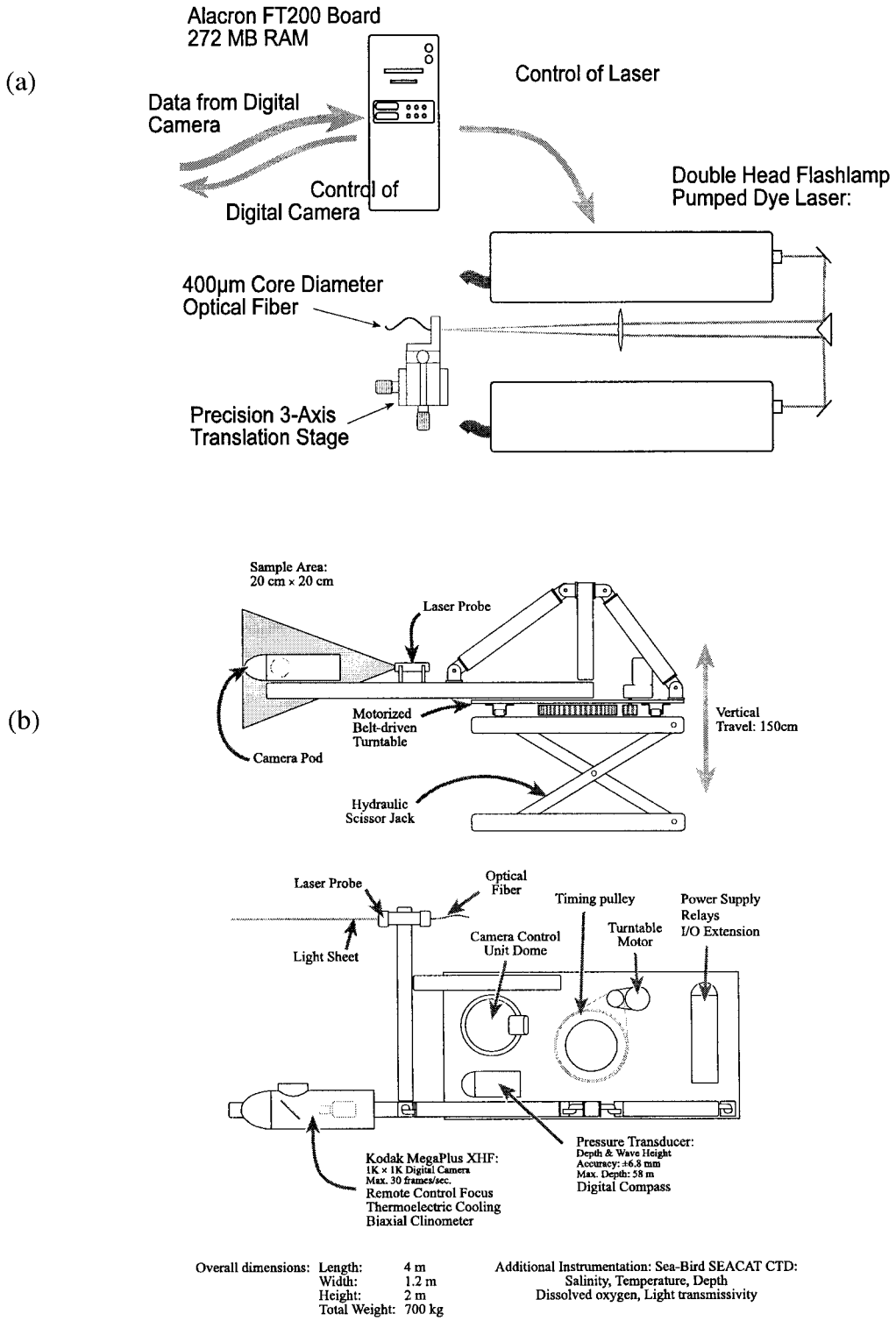

FIG. 1. Schematic views of the oceanic PIV system. (a) Surface-mounted laser, control and image acquisition subsystems. (b) Side and top views of the submersible instrument.

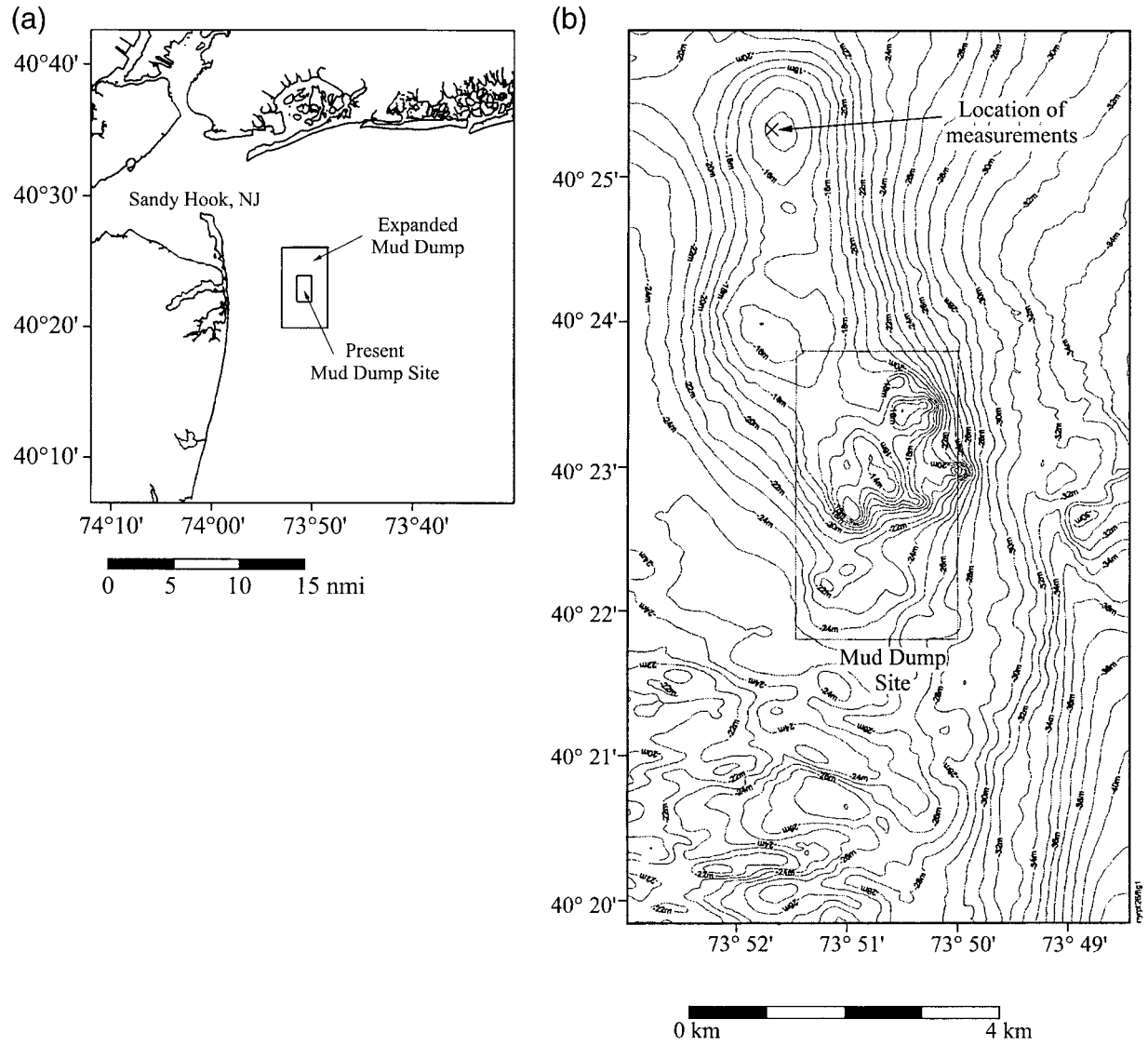

FIG. 2. (a) Location of the Mud Dump Site off the Sandy Hook, NJ, shore. Adapted from SAIC (1996), with permission. (b) Bathymetric contours of the test site at the Mud Dump Site off the Sandy Hook, NJ, shore. Isobaths are 1 m apart. The instrument is located near the 15-m isobath. Adapted from SAIC (1995), with permission.

acquired at the highest position ($118 < z < 138$), then at the lowermost ($10 < z < 30$), and then at gradually increasing elevations. A time delay between elevations of approximately 15 min was required for downloading the data, changing the elevation, and taking pressure readings for determination of the depth of the sample area.

3. Mean flow structure and sample vector maps

Prior to analysis, we first use the clinometer readings to determine the tilt at each elevation. The differences for the upper five stations are at most 0.2° (0.5° downwards at $z = 62$, 82, 106 cm, and 0.7° downwards at $z = 44$, 128 cm), which is the resolution limit of the tilt meter. Only at the bottom position the tilt is 0° (a difference of 0.58° relative to the average of the other stations—most likely because the tilt of the scissor-jack plate is slightly different when it is fully collapsed). Consequently, the vector maps of the bottom station are rotated to align the whole dataset in the same frame of reference.

We do not attempt here to minimize the vertical velocity, w, or its variance, separately for each measurement station, as suggested by Agrawal and Aubrey (1992). The normal velocity in a boundary layer should be exactly zero only at the seabed and different than zero at other elevations. In addition, large-scale bottom slope changes, bottom ripples, and external forcing (horizontal pressure gradients) also affect the

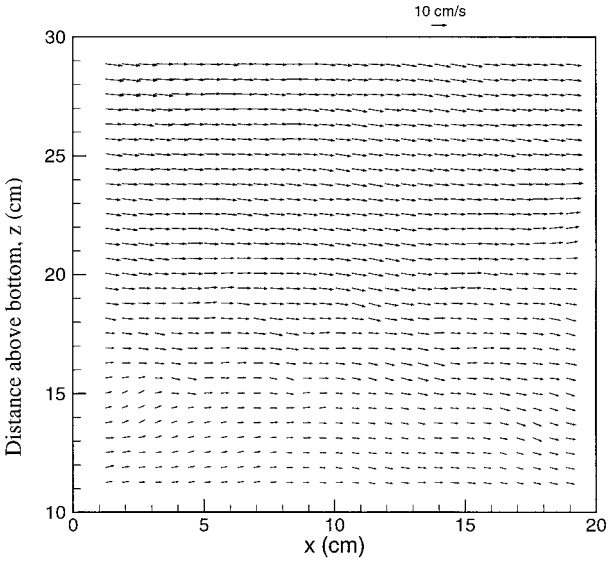

FIG. 3. Sample vector map at the lowest measurement station (the center is 20 cm above the bottom), constructed from two 1024 × 1024 pixel images taken 20 ms apart. The average horizontal velocity for this map is 4.83 cm s^{-1} at $z = 11.3$ cm, and 12.03 cm s^{-1} at $z = 28.7$ cm.

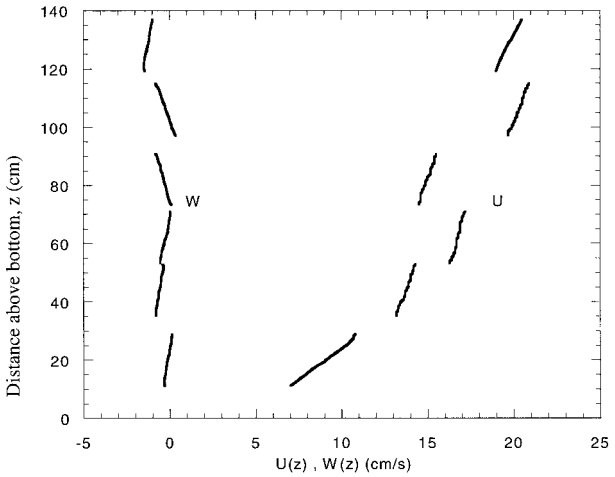

FIG. 4. Vertical distributions of mean horizontal (U) and vertical (W) velocities, calculated from 130 vector maps recorded at 1 Hz, at each of the six elevations. Time interval between measurement stations is 15 minutes.

vertical velocity. Our data indicates that the vertical velocity diminishes near the bottom (see Fig. 4), but does not vanish. Since the entire dataset is collected over a period of less than 90 minutes, we opt to maintain the same frame of reference for all the data.

The PIV data enables us to resolve the vertical velocity gradients within the image area, as demonstrated by the sample vector map at the lowest station shown in Fig. 3. The mean velocity components at a given elevation, $U(z)$ and $W(z)$ (horizontal and vertical components, respectively), are determined by averaging the data for that elevation over the 130 vector maps, that is,

$$U(z) = \frac{1}{130 \cdot 29} \sum_{n=1}^{130} \sum_{m=1}^{29} u(x_m, z, t_n) \qquad (1)$$

$$W(z) = \frac{1}{130 \cdot 29} \sum_{n=1}^{130} \sum_{m=1}^{29} w(x_m, z, t_n), \qquad (2)$$

where x_m and z define location within a certain vector map and t_n indicates maps recorded at different times. Thus, each value is an average of $29 \times 130 = 3770$ measurements. The resulting vertical distributions of mean horizontal and vertical velocity components are presented in Fig. 4.

The $U(z)$ distributions at the various stations do not form a continuous profile, although their slopes seem continuous. This behavior is most likely caused by time-dependent phenomena with timescales longer than the duration of the data series (130 sec). To illustrate this effect, each dataset is divided into five subsets, and calculating the mean velocity for each subset. As Fig. 5 shows, the mean velocity profile changes within each set, and the characteristics of the variations differ between measurement stations. For example, at $72 < z < 92$ cm, the mean flow accelerates nearly uniformly, whereas at $96 < z < 116$ cm, 15 minutes later, the flow first accelerates and then decelerates. Clearly, longer time series are necessary in order to obtain converged data. Near the bottom the vertical distribution of the horizontal velocity is nearly linear (Fig. 4). The gradient of $U(z)$ decreases but does not vanish with increasing elevation, as one would expect to find in a boundary layer over a flat surface. This trend indicates that the flow has mean shear at scales larger than the present measurement region. This shear persists for the whole duration of the test, that is, for more than an hour. The causes for this trend can only be resolved with measurements spanning a larger range of elevations, possibly the entire water column.

The time evolution of $U(z)$ and $W(z)$ is also demonstrated in Fig. 6, where each point represents an average velocity at a given elevation in one vector map. Each value is obtained by averaging over three rows of vectors (i.e., a ''strip'' 1.3 cm wide with the center at the indicated elevation). It is evident that the fluctuations in the time series consist of both the effects of (large scale) turbulence and wave-induced motion. As expected, the wave-induced orbital motion has more impact on the horizontal velocity (see also section 6). The irregularity of the fluctuations indicates the presence of large-scale turbulent structures, as well as nonlinearity of the waves and possibly the effect of multidirectional waves with different frequencies. In some cases, for example the mean hor-

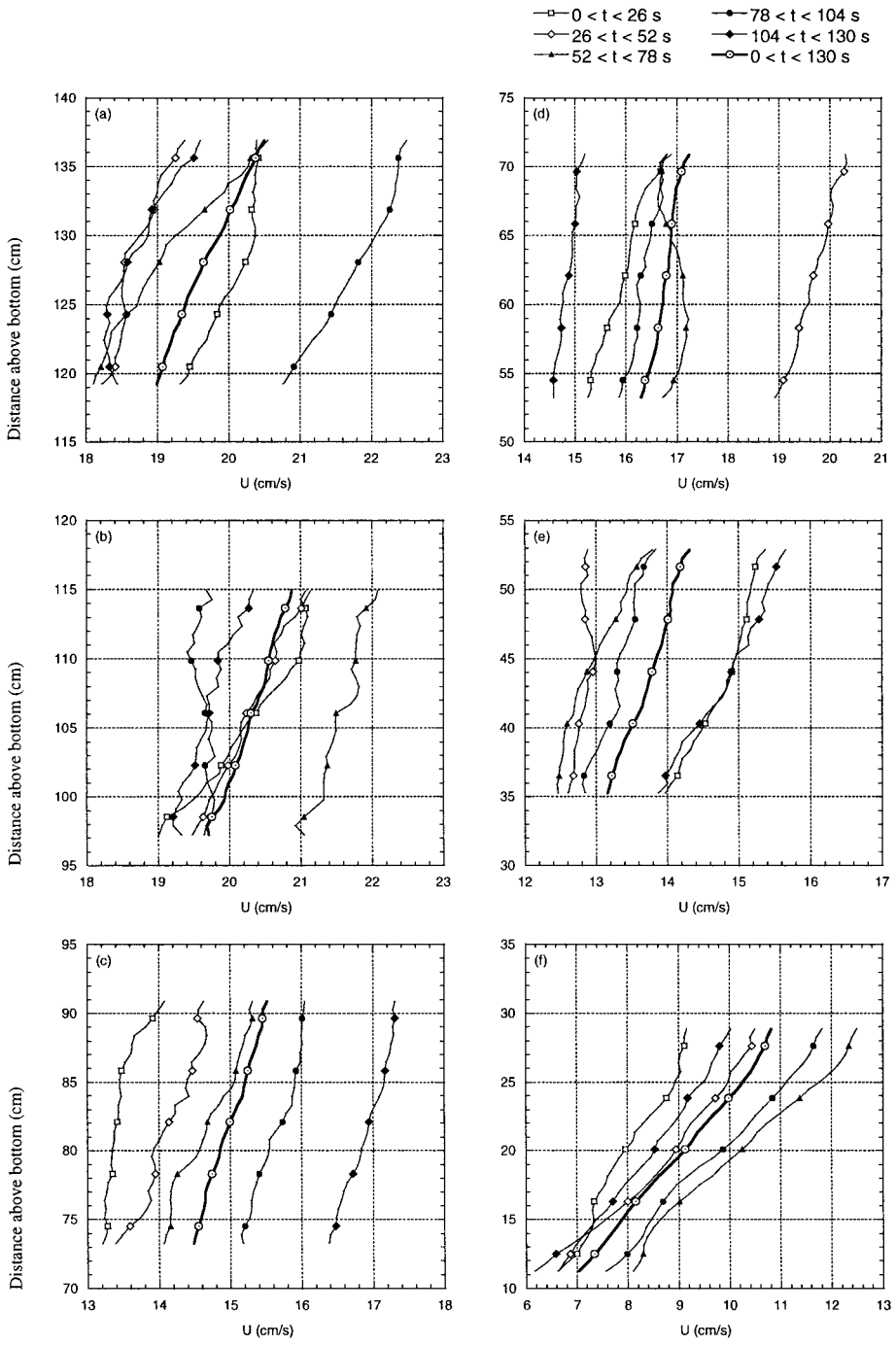

FIG. 5. Vertical distributions of mean horizontal (U) velocity, calculated for five subsets of 26 vector maps each (each point is the average of 754 vectors), and from the entire series of 130 vector maps recorded at 1 Hz, at each of the six elevations. The center of the sample area is at (a) $z = 128$ cm, (b) $z = 106$ cm, (c) $z = 82$ cm, (d) $z = 62$ cm, (e) $z = 44$ cm, (f) $z = 20$ cm.

izontal velocity at $z = 62$ cm, there are clear temporal variations at scales much longer than the duration of the present tests.

To demonstrate the characteristic structure of the turbulence and that structures can be identified as they are convected between successive realizations, we present in Figs. 7a–d sample sequence of four vector maps with distributions of $u(x, z, t) - U(z)$ and $w(x, z, t) - W(z)$. For example, the structures denoted 1 and 2 are convected by about half a frame between realizations, consistent with the mean velocity of about 9 cm s^{-1} at $z = 20$ cm. In Figs. 7e and 7f, taken from the highest

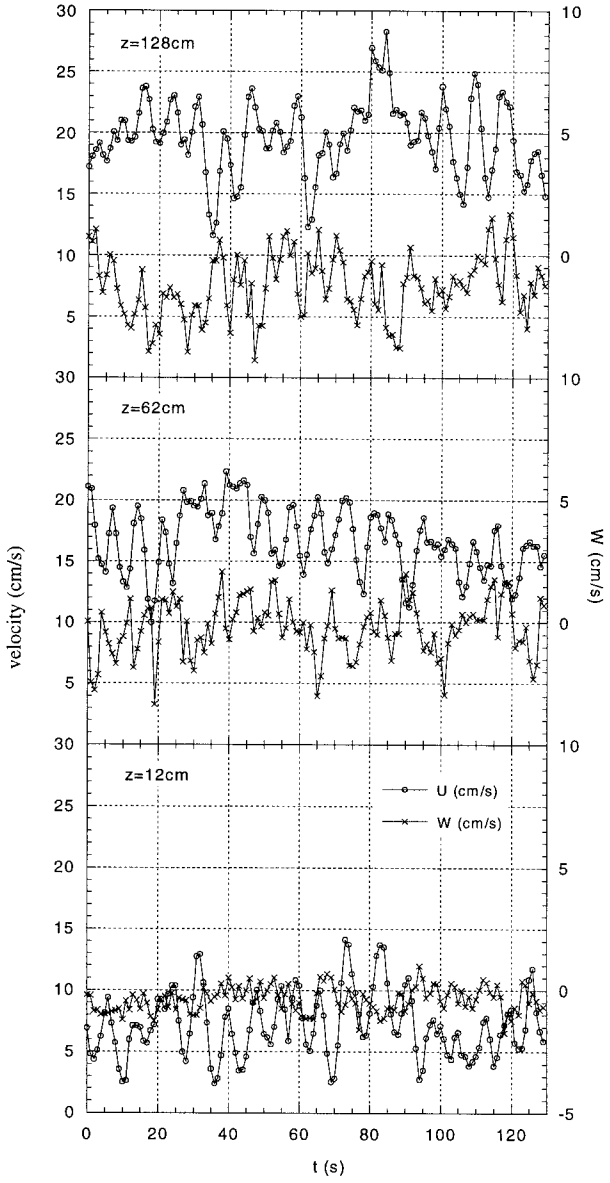

FIG. 6. Time evolution of the mean velocity at different elevations. Each point on the figure is the average of data from a 1.3 cm "strip" centered at the given elevation (i.e., the average of $3 \times 29 = 87$ measured data points).

measurement station, one can identify small eddies embedded within larger structures.

4. Spatial energy and dissipation spectra of turbulence

To obtain a 1D spectrum, one has to evaluate the Fourier transform:

$$F_i(k_1, z_j) = \sum_n u_i(x_n, z_j)W(x_n, z_j) \exp(-ik_1x_n);$$

$$F_i(k_3, x_j) = \sum_n u_i(x_j, z_n)W(x_j, z_n) \exp(-ik_3z_n), \quad (3)$$

where u_i and k_i are the velocity and wavenumber in the i direction ($i = 1$ is the horizontal direction and $i = 3$ is the vertical direction in the vector map frame of reference), at coordinate (x_n, z_n), and $W(x_n)$ is a windowing function. The subscript j is fixed for a specific operation. The spectral density is then calculated from

$$E_{ii}(k_1, z_j) = \frac{L}{2\pi N^2} \sum_n F_i(k_1, z_j)F_i^*(k_1, z_j);$$

$$E_{ii}(k_3, x_j) = \frac{L}{2\pi N^2} \sum_n F_i(k_3, x_j)F_i^*(k_3, x_j), \quad (4)$$

where L is the domain length, N is the number of points, and F_i^* is the complex conjugate of F_i.

We calculate the spectral density of the instantaneous velocity from individual vector maps both in the horizontal and vertical directions. The procedures include prewhitening (i.e., creating a series of first differences, whose spectra are converted back to the spectra of the original data), subtraction of mean value, and zero padding symmetrically on both sides of the 28 data points to extend the series to 32 points. A Hanning windowing function and scaling to compensate for energy loss due to Hanning, that is, maintaining the variance assuming a uniform distribution, are used for alleviating end effects. Comments on the effect of these processing procedures on the results are introduced in section 5b. Results from 130 vector maps at the same elevation are averaged. In addition, to increase the number of points being averaged in the horizontal spectra $[E_{ii}(k_1, z_j)]$, results of three adjacent rows are also averaged. Similarly, data for $E_{ii}(k_3, x_j)$ are averaged over three columns. For brevity, we omit x_j and z_j in the following discussions.

Sample spatial spectra are presented in Figs. 8a and 8b, the former containing horizontal spectra, that is, $E_{11}(k_1)$ and $E_{33}(k_1)$, and the latter containing vertical spectra, $E_{11}(k_3)$ and $E_{33}(k_3)$. The error bars indicate the 95% confidence level range. Note that these results represent true spatial spectra and do not involve use of the Taylor hypothesis. The results are compared to the Nasmyth universal spectrum for isotropic turbulence using data provided in Oakly (1982). The dissipation rates of the universal curves are chosen to match $E_{11}(k_1)$ at low wavenumbers. The spectra are then multiplied by k^2 and replotted to show dissipation spectra (Tennekes and Lumley 1972). Sample representative distributions for the six elevations of $k_1^2E_{11}(k_1)$, $k_1^2E_{33}(k_1)$, $k_3^2E_{33}(k_3)$, and $k_3^2E_{11}(k_3)$ are presented in Figs. 9a–d, respectively.

Several trends are clearly evident from the results in Figs. 8 and 9. First, for all the cases shown the data cover part of the inertial range of turbulence (slope $\sim -5/3$) but extend well into the dissipation range. Second, the turbulence is anisotropic over the entire range covered by these spectra. Starting with Fig. 8a, at low wavenumbers ($k_1 < 150$ rad s^{-1}) $E_{33}(k_1)$ is clearly larger than the universal isotropic turbulence values. The en-

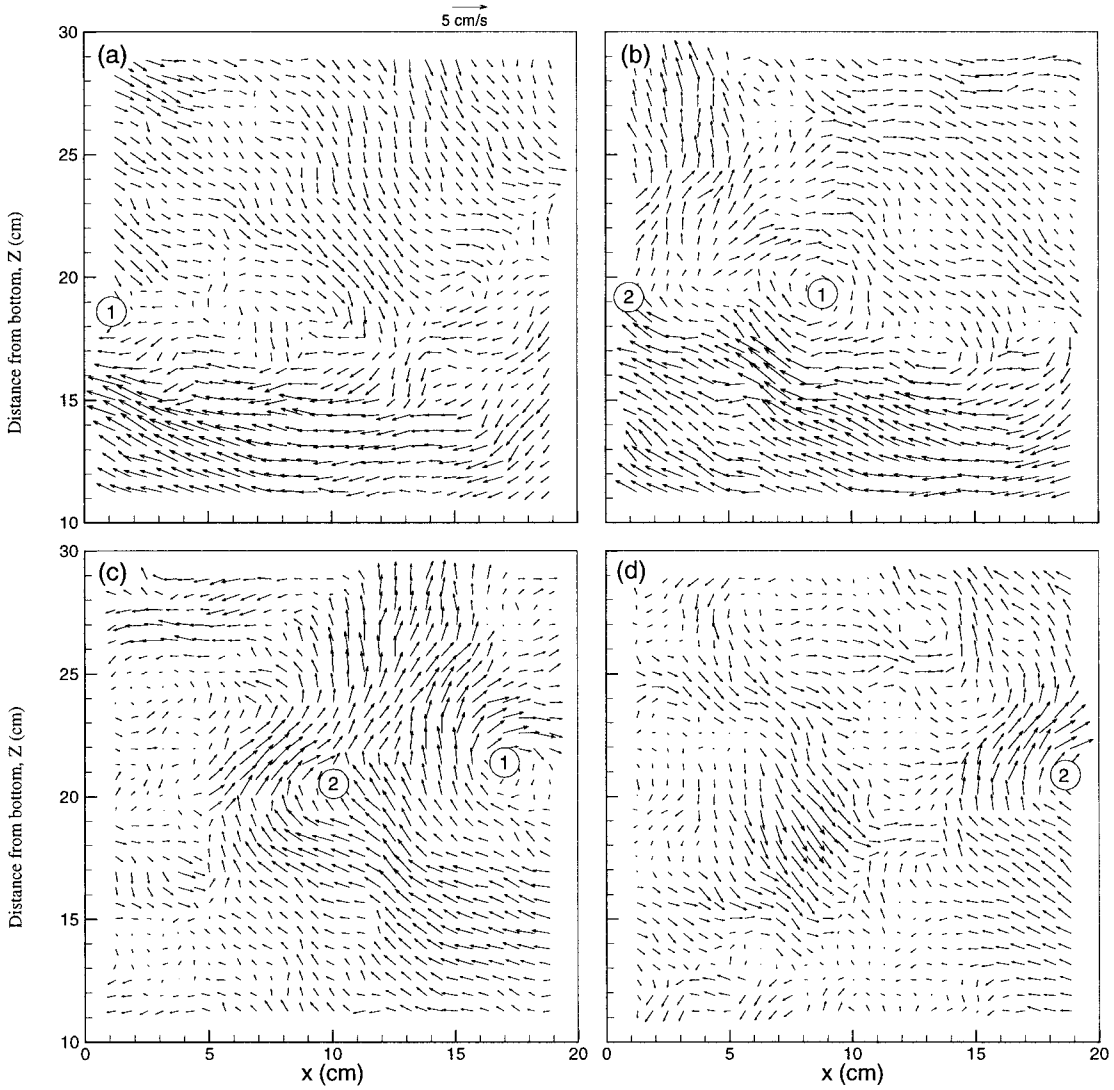

FIG. 7. Vector maps of velocity fluctuations {[$u(x, z, t) - U(z)$], [$w(x, z, t) - W(z)$]}. [(a)–(d)] Sequence of four maps, measured at 1-s intervals, at the lowest station. Note the structures designated as 1 and 2 being convected across the sample area. [(e), (f)] Sample individual maps, at the highest measurement station.

ergy at low wavenumbers in Fig. 8b is different from the results in Fig. 8a, but still $E_{33}(k_3) > 0.75E_{11}(k_3)$, unlike isotropic turbulence spectra. At high wavenumbers both longitudinal spectra [$E_{11}(k_1)$, $E_{33}(k_3)$] display peculiar trends that, to the best of our knowledge, have never been reported before. In the range $150 < k_i < 250$ (all wavenumbers are in rad s^{-1}) both have ''humps'' after which $E_{11}(k_1)$ matches the values of $E_{33}(k_1)$, and $E_{33}(k_3)$ matches the values of $E_{11}(k_3)$. In other words, the spectra of the velocity component parallel to the wavenumber have very similar humps, whereas the spectra of the component normal to the wavenumber do not. This trend is independent of the direction relative to the mean flow.

In searching for a plausible explanation for this phenomenon, the option of noise/error in the data is rejected since data for the same velocity component and from the same vector map are used for calculating both $E_{11}(k_1)$ and $E_{11}(k_3)$ and for both $E_{33}(k_1)$ and $E_{33}(k_3)$. The humps, on the other hand, exist only in the longitudinal spectra and not in spectra of the velocity component normal to the wavenumber (irrespective of its direction). This trend is also not an artifact of the detrending or windowing procedures, since it is observed even when no windowing or detrending is applied. At this stage we do not have an explanation for this trend. One possibility may be the ''bottleneck effect'' (e.g., Falkovich 1994; Lohse and Muller-Groeling 1995), which is also observed experimentally in high Reynolds number boundary layer flow (Saddoughi and Veeravalli 1994). Another could be narrowband noise caused by an as yet unidentified source. Note that Voulgaris and Trowbridge

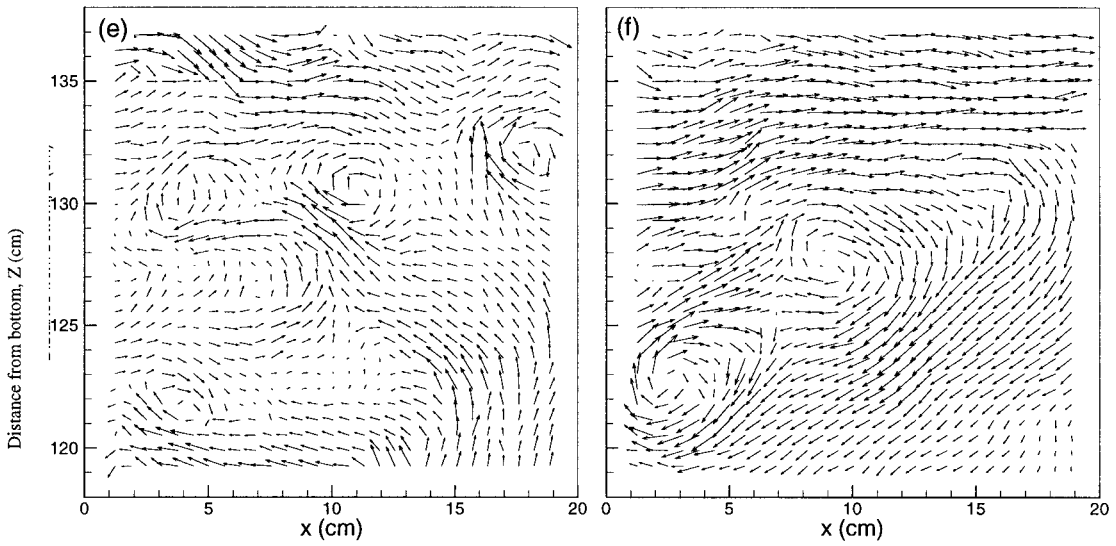

FIG. 7. (*Continued*)

(1998) report similar trends with ADV data, which they attribute to effects of viscous dissipation, production, attenuation due to spectral averaging over the ADV sample volume, and measurement noise.

The dissipation spectra in Fig. 9 accentuate the systematic difference between spectra of velocity components that are parallel and those that are perpendicular to the wavenumber. At five of the six elevations, the dissipation spectra of the normal velocity components have peaks at $100 < k_i < 250$ (Figs. 9d,c). Although one may detect a change of slope at the same wavenumber range in the spectra of the parallel component, which indicates the presence of a local maximum, the dominant peaks are located in the $250 < k_i < 350$ range.

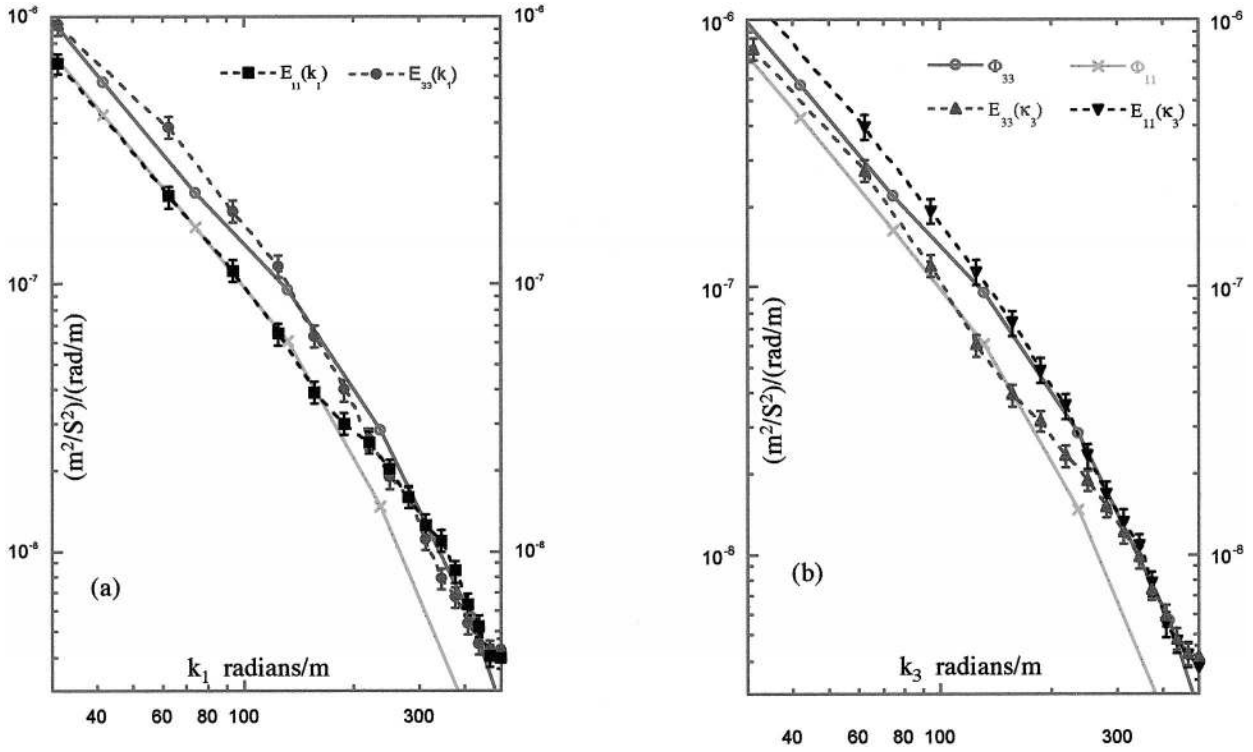

FIG. 8. Measured true spatial energy spectra compared to the Nasmyth universal spectrum (Oakly 1982), ϕ_{11} and ϕ_{33} calculated using $\epsilon = 8 \times 10^{-6}$ m^2 s^{-3} [to match $E_{11}(k_1)$ in the inertial range]. (a) $E_{11}(k_1)$ and $E_{33}(k_1)$. (b) $E_{11}(k_3)$ and $E_{33}(k_3)$. The experimental results are based on averages of three rows (or columns) from 130 instantaneous realizations.

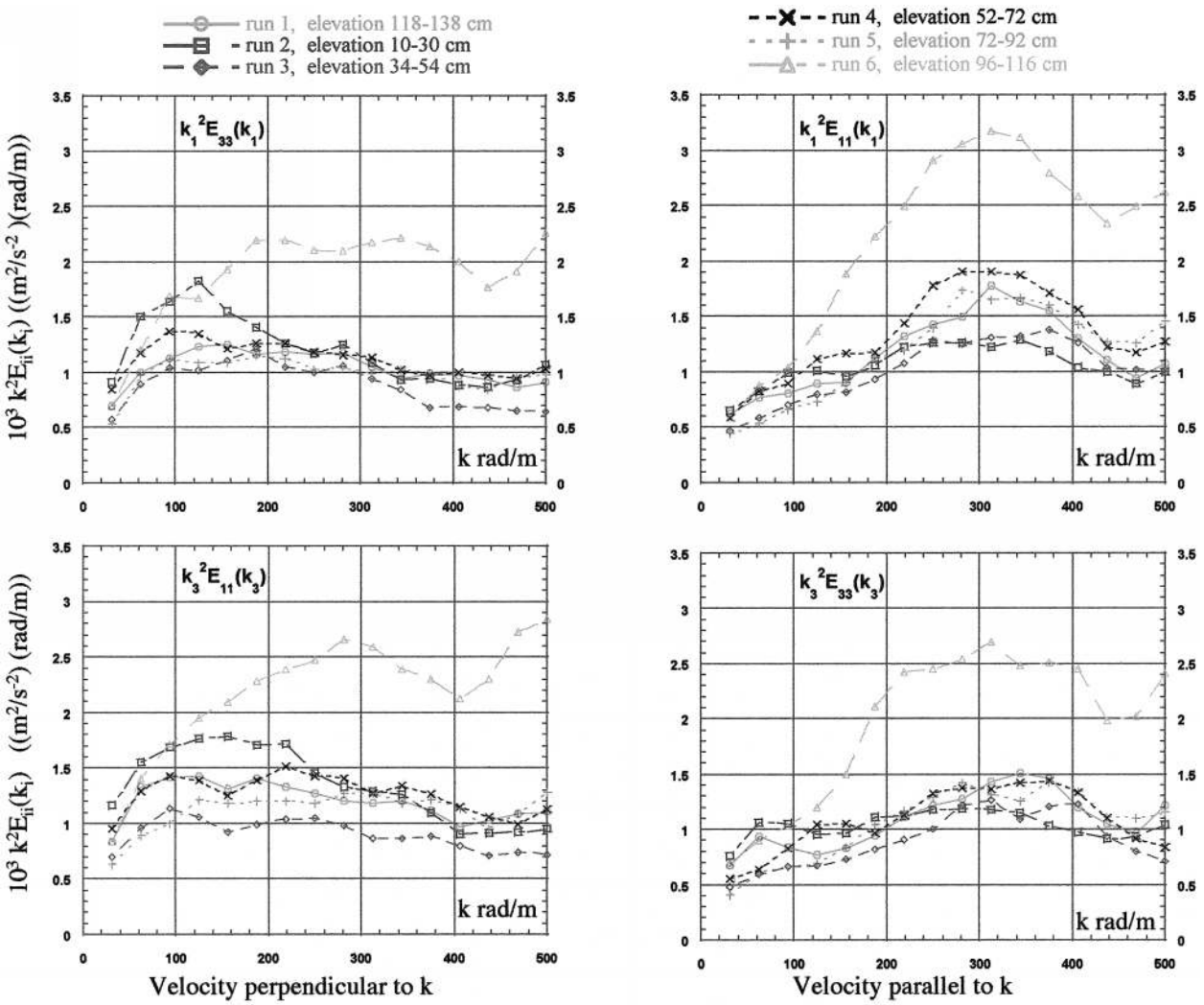

FIG. 9. Spatial dissipation spectra at different elevations. Each line is an average over three rows (or columns) and 130 vector maps.

Thus, for five of the six elevations, trends are consistent. We'll later use integration of the dissipation spectra as one of the methods for estimating the rate of dissipation.

The only exception is the data for $96 < z < 116$ (all dimensions are in cm), the last dataset recorded and one station below the highest elevation. For this case the dissipation spectra have substantially higher magnitudes and both parallel and normal components have peaks at $250 < k_i < 350$. There is also either a clear peak or a small change of slope (kink) at $k_i \approx 200$. Since the measurements at different elevations are performed at different times, it is possible that the difference is caused by changes in the flow conditions at the time of the measurements. Since no measured tide data is available for the test site (40.42°N, 73.86°W) at the time of the experiment, we use Nautical Software, Inc. (1998) to estimate the variations of the tidal current at the nearest available locations. Most notably, the tide reverses direction between 1233 and 1246 UTC. Our measurements at this elevation took place between 1302 and 1304 UTC (the previous five sets were recorded between 1145 and 1248 UTC). Thus, the change is consistent with tidal changes.

5. Extended data series using the Taylor hypothesis

a. Interpolation of vector maps

Up to the scale of a vector map we have calculated the spectra based on the measured instantaneous spatial velocity distributions. In order to resolve longer scales, the time series of vector maps is converted into a spatial series using Taylor's hypothesis. The procedure is introduced in Bertuccioli et al. (1999), but due to its significance this paper repeats the method used to combine the discrete vector maps into an extended composite map.

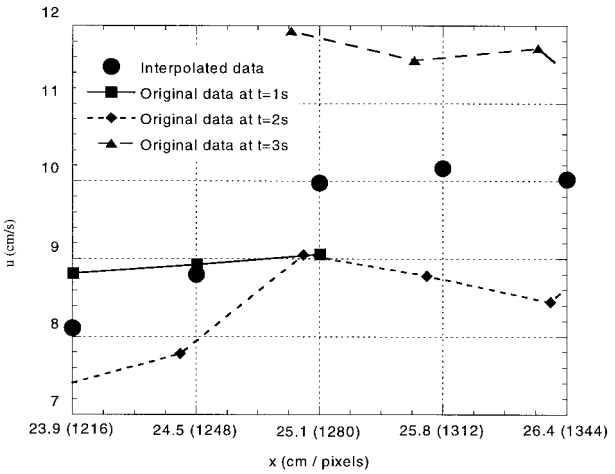

FIG. 10. Illustration of the velocity interpolation method from original data onto a regularly spaced grid. The interpolated u at $x = 25.1$ cm is the weighted average of six original data points from three consecutive vector maps, lying between $x = 24.5$ cm and $x = 25.8$ cm. The interpolated u at $x = 24.5$ cm is the weighted average of five original data points (two from $t = 1$ s, two from $t = 2$ s, and one from $t = 3$ s), lying between $x = 23.9$ cm and $x = 25.1$ cm.

For each individual vector map we estimate the average horizontal velocity in a ''strip'' 1.3 cm wide (three rows of vectors) around the desired elevation. This average advective velocity is used to evaluate the displacement between successive vector maps. At the lowest elevation ($z = 12$ cm) the displacement between vector maps is 2.6–13.9 cm (132–709 pixels) with an average of 7.3 cm (373 pixels), and there is considerable overlap between maps, as the samples in Fig. 7 show. At the highest elevations the overlap is very small. At $z = 106$ cm (the elevation with the largest mean current) only 55% of the vector maps overlap at all, and the displacements range between 14.2 and 26.4 cm (725–1346 pixels), with an average of 20.3 cm (1035 pixels). In cases where there is a gap between successive vector maps, we need to fill in the missing data using linear interpolation. The typical gap is 1–3 vector spacings, with a maximum of 10 vector spacings. Such gaps occur only for the two highest measurement stations. The effect of the interpolation on the spectra is discussed and demonstrated in section 5b.

In cases with overlap the neighboring vector arrays at a specific elevation are interleaved using the appropriate convection velocity to yield an irregularly spaced ''spatial'' series consisting of $130 \times 29 = 3770$ points, x_j. This data is then interpolated onto a regularly spaced array, X_i, where the spacing between consecutive points is equal to the spacing between vectors in the individual maps, s (i.e., $s = 0.63$ cm). Each point on the regular array is assigned a velocity, $[u^{\text{int}}(X_i), w^{\text{int}}(X_i)]$, which is equal to the weighted average of the original data points within a range whose width is equal to that of an interrogation window ($2s$). Thus:

TABLE 1. The number of interpolated points in the extended data series and the corresponding series lengths.

Elevation (cm)	Number of points in extended data series, N_{TOT}	Length of extended data series recorded over 130 s at 1 Hz (m)	Number of points for FFT, N_{FFT}
128	4063	25.4	2048
106	4202	26.2	4096
82	3102	19.3	2048
62	3464	21.6	2048
44	2846	17.7	2048
12	1533	9.6	1024

$$u^{\text{int}}(X_i) = \left.\frac{\sum (s - |x_j - X_i|)u(x_j)}{\sum (s - |x_j - X_i|)}\right|_{|x_j - X_i| < s} \quad (5)$$

$$w^{\text{int}}(X_i) = \left.\frac{\sum (s - |x_j - X_i|)w(x_j)}{\sum (s - |x_j - X_i|)}\right|_{|x_j - X_i| < s}. \quad (6)$$

A sample case from the $z = 12$ cm data is shown in Fig. 10. The region 23.9 cm (1216 pixels) $< x <$ 26.4 cm (1344 pixels) on the irregular grid includes velocities from three successive realizations. Hence, $u^{\text{int}}(X = 25.1$ cm) is the weighted average of the velocities at six points of the original irregular grid, whereas $u^{\text{int}}(X = 24.5$ cm) and $u^{\text{int}}(X = 25.8$ cm) are each the weighted average of five original data points. Using this procedure, we generate a Taylor-hypothesis-based ''spatial'' series of two velocity components at selected elevations. The total lengths of these patched and interpolated distributions vary with elevation due to the different convection velocities, as summarized in Table 1.

b. Evaluation of interpolated spectra

Spectral densities for u' and w' [$E_{11}(k_1)$ and $E_{33}(k_1)$, respectively] are calculated using the regularly spaced interpolated arrays. To take advantage of an entire dataset with N_{TOT} points, without zero padding and still obtain a number of points equal to 2^n, each $u^{\text{int}}(X)$ and $w^{\text{int}}(X)$ distribution is divided into two subsets of N_{FFT} points (values are provided in Table 1). The first subset contains the data at X_i, where $0 \le i \le N_{\text{FFT}} - 1$, and the second contains the data at X_i, where $N_{\text{TOT}} - N_{\text{FFT}} \le i \le N_{\text{TOT}} - 1$.

Three methods have been tested for detrending the data series (Emery and Thomson 1997): Subtraction of the series average, linear detrending (removing a best-fitted linear curve), and prewhitening (using a series of first differences and conversion to spectra of the original data). Two windowing functions have been used: a Hanning window and a cosine tapered windowing function (applied to the first and last 10% of the data series, while keeping the rest of the data unchanged). The windowed data series is scaled to compensate for energy ''loss'' due to application of the windowing function. For a

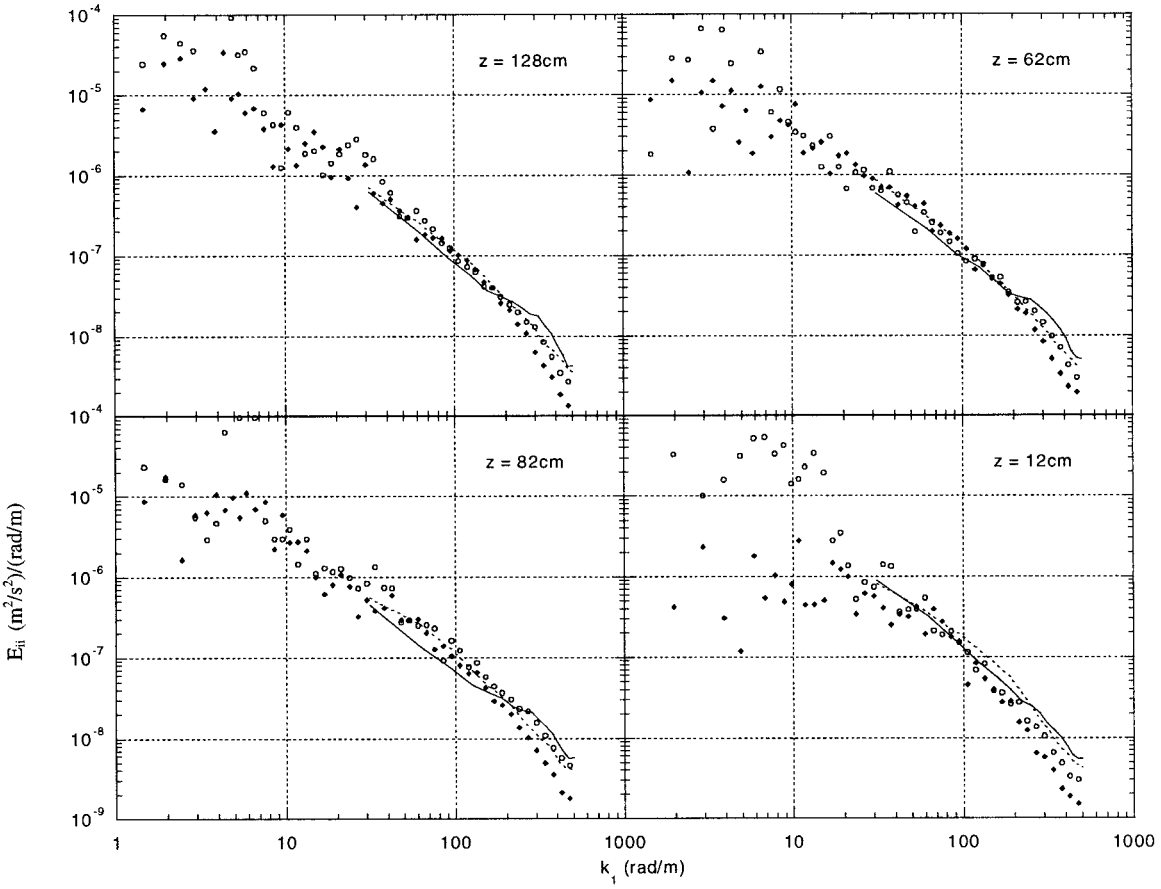

FIG. 11. A comparison between spectra obtained using true spatial (TS) data and extendedinterpolated (EI) data. Solid lines: TS E_{11}, dotted lines: TS E_{33}; solid symbols: EI E_{11}; open symbols: EI E_{33}.

continuous form of the windowing function, the scaling coefficient is $\sqrt{8/3} = 1.633$ for the Hanning window and 1.084 for the 10% cosine tapered window. For the discrete case, the exact value of the scaling factor depends on the number of points. Note that the variance of the raw data is conserved only if the data is fully uncorrelated to the window. In the present case, the data is not white, and the length of the data series is not sufficient to ensure decorrelation. Hence, application of a windowing function results in some loss of variance, even after scaling.

Using the present data and comparing the results we have found that the spectra obtained using different windowing functions and detrending procedures are very similar except for the lowest wavenumbers. In this range the spectra are determined from very few points and the associated level of confidence is small. Consequently, we opt to use prewhitening and cosine tapered windowing for the patched–interpolated data series. As noted before, a Hanning window is used for computing the spectra of individual vector maps.

Using the two subsets of data, spectra of u' and w' are evaluated at each elevation. These spectra are then averaged to yield $E_{11}(k_1, z)$ and $E_{33}(k_1, z)$. In order to increase the amount of data used for each spectrum, we also average data from three successive vector rows, that is, a 1.3-cm vertical band. The results are then band averaged onto a grid of 20 bins per decade. Thus, at the low wavenumbers the actual data points are plotted, whereas at the highest wavenumbers each point on the plot is an average of 50–200 calculated points. This binning does not affect the trends of the spectra, but it decreases the fluctuations of the curves. To the best of our knowledge this method of patching PIV data using the Taylor hypothesis to obtain extended spectra has been introduced for the first time in our previous paper (Bertuccioli et al. 1999). Thus, before presenting the results, the extended spectra are compared to the true spatial spectra obtained from instantaneous maps in the wavenumber range that they overlap.

c. Impact of vector map interpolation on spectra

True spatial spectra averaged over 130 vector maps and three adjacent rows (denoted TS in the following) are compared to the spectra obtained with the extended and interpolated data (denoted EI) in Figs. 11 and 12. The TS spectra are not band averaged, as each individual

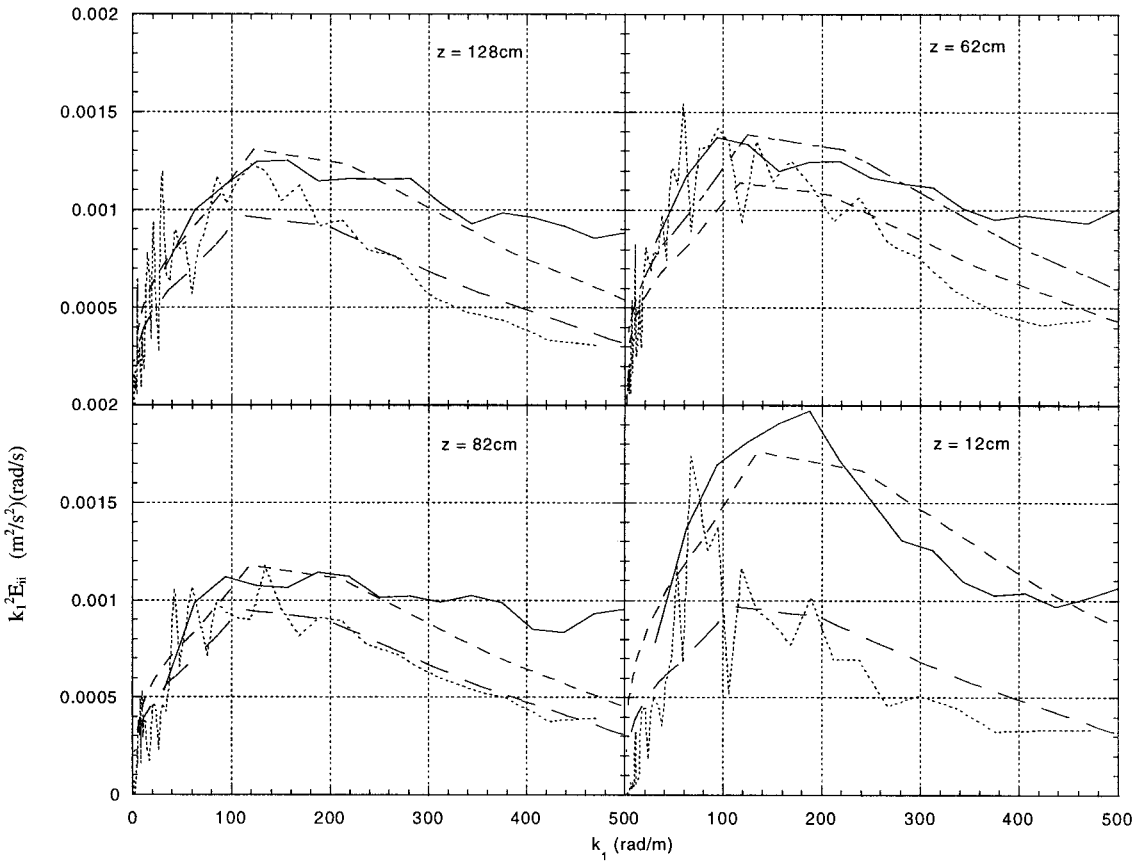

FIG. 12. A comparison between dissipation spectra obtained using TS data and EI data. Solid lines: TS $k_1^2E_{33}$; dotted lines: EI $k_1^2E_{33}$; dashed lines: Nasmyth universal spectra.

spectrum contains only 16 points. Their smooth curves are a result of being averages of 130 individual spectra. As is evident, the energy spectra are similar in the low wavenumber part of the overlapping range, whereas at large wavenumbers the extended series contains less energy. This trend is also observed in the data of Bertuccioli et al. (1999). The humps in $E_{11}(k_1)$ at high wavenumbers ($k_1 \approx 200$ rad m^{-1}), which are evident in the TS spectra and discussed in section 4, also exist in the EI spectra but to a lesser extent.

In order to provide a quantitative measure for the differences, the total energy contents in the range of overlapping wavenumbers are calculated using.

$$e_i = \int E_{ii}\, dk_1, \qquad i = 1, 3. \tag{7}$$

Results are presented in Table 2. The TS spectra of vertical velocity contain more energy than the EI spectra, with the largest difference (55%) occurring near the bottom. At the other elevations the differences are smaller (10%–30%). The TS horizontal velocity spectra contain more energy than the corresponding EI spectra at low elevations, but the trend is reversed at the higher elevations. Overall, the differences range from 5% to 20%.

Two effects contribute to these trends: First, at low elevations, there is considerable overlap between vector maps, resulting in some filtering of the high wavenumber energy due to the interpolation scheme. The overlap (and hence the interpolation-induced smoothing) is reduced away from the bottom. Second, as discussed in sections 5d and 7, surface-wave-induced motion has substantial effect on the extended data series and spectra. The characteristic timescales of the waves and of the energy containing turbulent eddies are similar

TABLE 2. Energy content in the range of wavenumbers where the averaged true spatial spectra (TS) and the extended vector maps (EI) overlap.

Elevation (cm)	Average of true spatial spectra (TS)		Extended/interpolated series (EI)	
	$e_1 \times 10^5$ (m² s^{-2})	$e_3 \times 10^5$ (m² s^{-2})	$e_1 \times 10^5$ (m² s^{-2})	$e_3 \times 10^5$ (m² s^{-2})
128	3.6	3.7	3.8	2.9
106	4.4	4.3	5.5	3.9
82	2.8	3.0	3.8	2.7
62	3.6	4.4	3.6	3.6
44	3.1	3.0	2.6	2.3
12	4.6	4.5	4.1	2.9

(but not the wavelength). Hence, in the extended series, constructed using the Taylor hypothesis, the wave-induced motion appears at equivalent wavenumbers (see section 7) of 2–10 rad m^{-1} and leaks to higher harmonics, that is, to the range where we compare the TS and the EI spectra (k_1 = 31–500 rad m^{-1}). The TS spectra, on the other hand, are based on measured spatial distributions within individual vector maps. There is a significant difference between the length scale of the measurement area (20 cm) and the wavelength of the surface waves (e.g., in water 15 m deep, a wave with a 7.5 s period has a wavelength of 75 m). Due to this more than two orders of magnitude separation of length scales, the TS spectra are affected very little by wave-induced motion. The wave effect on the horizontal velocity is more significant than on the vertical velocity (see section 7), especially as the bottom is approached. Consequently, the E_{33} spectra are influenced mostly by the interpolation, which is most significant near the bottom. Also, the wave-induced motion introduces more energy into the EI spectra of E_{11} at high elevations. The largest difference between the EI and TS horizontal spectra occurs at z = 82 cm, where the wave spectral peak is most pronounced.

The increasing difference between the TS and EI spectra with increasing wavenumbers are accentuated in the dissipation spectra, especially when plotted in linear scales (Fig. 12). Due to the interpolation, the difference is particularly high near the bottom. When compared to the universal spectrum, it appears that the EI spectra match the universal spectral shape more closely than the TS spectra, which exhibit a roll-off at k_1 = 200–300 rad m^{-1}. This trend is most likely a result of higher noise contamination in the TS spectra at high wavenumbers (Bertuccioli et al. 1999). This noise is partially filtered out by the interpolation. Figure 12 indicates that dissipation rate estimates based on integration of TS and EI dissipation spectra (see section 6) will give different results. However, since most of the deviations occur in the high wavenumber region, dissipation estimates calculated with a line fit of a $k^{-5/3}$ curve to the inertial range are in closer agreement than those evaluated from an integral of the dissipation spectrum. A comparison between dissipation estimates for the two datasets using various prediction methods is discussed in section 6.

d. Interpolated velocity spectra

Sample extended and interpolated spectra for several elevations are shown in Fig. 13. The Nasmyth universal spectrum, based on the numerical values given by Oakey (1982) is also included. The range of resolved wavenumbers spans about three decades, except near the floor, where it is slightly smaller. The spectra contain only small regions with horizontal tails (that are characteristic of high-frequency white noise), at $k_1 > 400$ rad m^{-1}, corresponding to wavelengths of less than 1.6 cm. At the large scales ($k_1 < 8$), E_{11} is greater than E_{33} at all elevations. These scales contribute most of the velocity variance, which has a typical ratio of $u'^2/w'^2 \sim 4$ (section 8). The substantially larger energy content of the horizontal velocity fluctuations is due to both the anisotropy of the turbulence and the effect of wave-induced motion. The latter is discussed and compared to spectra of surface waves in section 7. The effect of the anisotropy extends to low wavenumbers that are beyond the range contaminated by the surface wave spectral peaks.

The difference between E_{11} and E_{33} is most significant near the seafloor, at z = 12 cm and decreases as the distance from the bottom increases to 44 cm and then to 62 cm. At higher elevations the difference remains at about the same level. Although E_{11} changes shape considerably at low wavenumbers (due to the wave effect), the characteristic peak magnitudes remain at similar levels at all of the measurement stations. The levels at low wavenumbers are all in the 10^{-5}–10^{-4} $(m^2\ s^{-2})/(rad\ m^{-1})$ range and the wave-induced peaks exceed 10^{-4}, except for the lowest elevation. On the other hand, the characteristic peak magnitude of E_{33} decreases by more than an order of magnitude between z = 128 cm and z = 12 cm. Thus, the energy content of the vertical velocity fluctuations is reduced when approaching the bottom, whereas the energy content of the horizontal velocity fluctuations is not affected substantially by the elevation. This trend most likely indicates the presence of large-scale horizontal eddies (with vertical axes), whose sizes do not depend on elevation (as well as the wave contamination). In contrast, the characteristic size of vortices with horizontal axes decreases as the floor is approached. This trend has been observed in laboratory turbulent boundary layer measurements, and has traditionally led to the use of the distance from the wall as an estimate for the integral length scale, l, for boundary layer flow. This integral length scale can be estimated from the measured vertical spectra using the wavenumber in which transition away from the inertial range ($-5/3$) slope occurs. For example, at z = 12 cm the vertical velocity spectrum flattens at about $k_1 \approx 40$ rad m^{-1}, that is, l = 16 cm (Fig. 13), and at z = 82 cm the flattening occurs at a wavenumber of about 8, corresponding to $l \approx 80$ cm. Unfortunately, the flattening is partially obscured by the spectral peak induced by the surface wave.

For small scales the differences between E_{11} and E_{33} decrease (but do not disappear). Least squares fits to the data in the range where it seems to be parallel to a $-5/3$ slope yield the coefficients A_{ii} shown in Table 3, where $E_{ii} = A_{ii}k_1^{-5/3}$. In all cases the range of wavenumbers where a $-5/3$ slope line can be fitted is small and does not exceed a decade. At the lowest station (z = 12 cm), this range is even smaller, reducing the confidence level of the line fit. For isotropic turbulence, in the inertial range, $E_{11}(k_1) = \frac{3}{4}E_{33}(k_1)$. Clearly for the present data this ratio is not satisfied, supporting the results obtained with the true spatial spectra (section 4), that the turbulence is not isotropic. The extended data shows that the anisotropy extends to the entire spectrum.

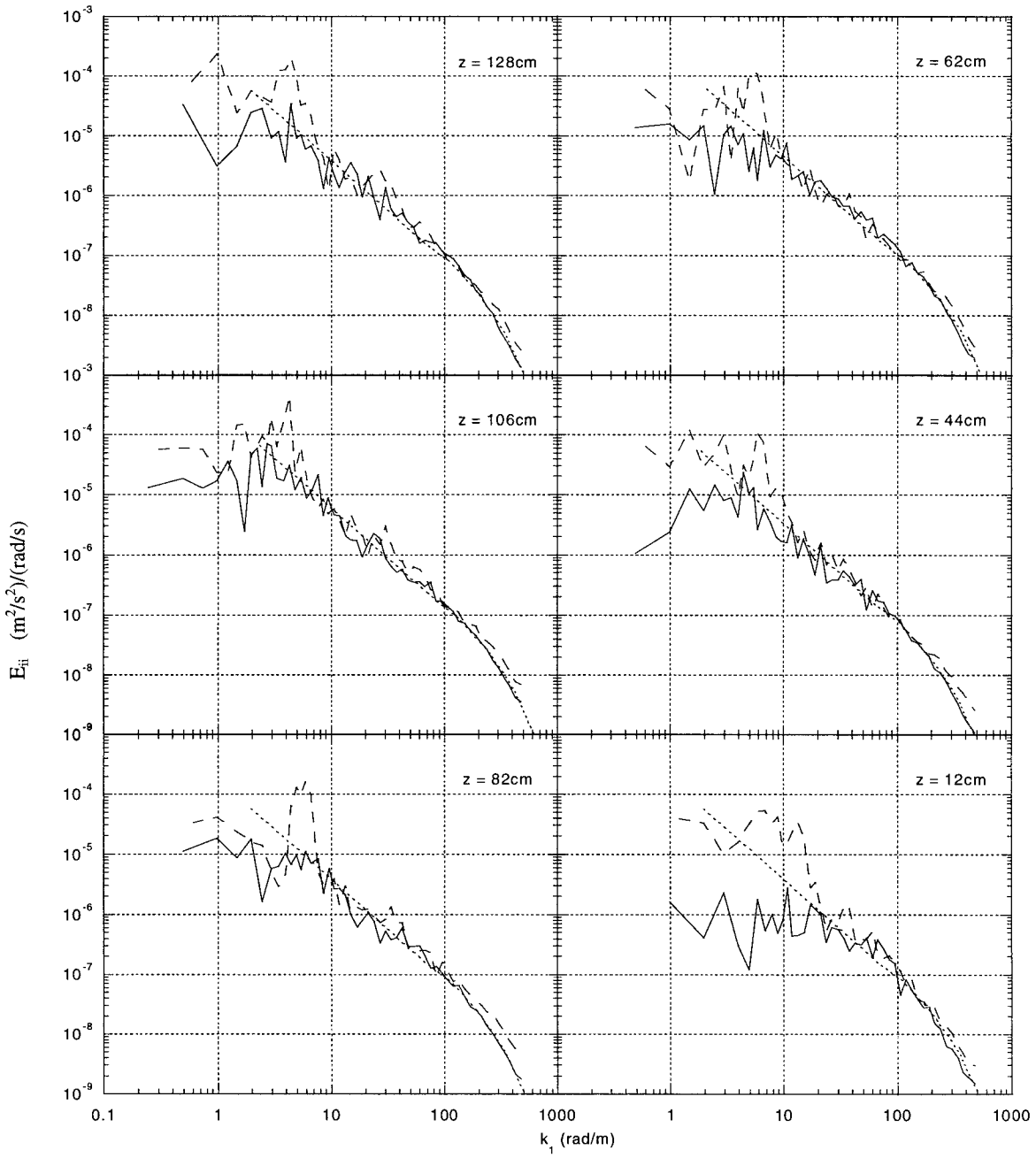

FIG. 13. Sample spectra of turbulent velocity fluctuations, calculated from the extended and interpolated vector maps. Solid lines: E_{33}; dashed lines: E_{11}; dotted lines: Nasmyth universal spectrum [which has a $-5/3$ slope in the inertial range], fitted based on the dissipation spectra of the vertical velocity component.

TABLE 3. Results of least squares best fit to ($-5/3$) slopes at intermediate wavelength for the sample spectra in Fig. 13.

Elevation (cm)	$A_{11} \times 10^4$	$A_{33} \times 10^4$
128	2.2	2.3
106	3.5	3.0
82	2.4	2.1
62	2.5	2.6
44	1.8	1.7
12	2.3	1.9

6. Rate of kinetic energy dissipation

Sample ''dissipation spectra'' (Tennekes and Lumley 1972), that is, plots of $k_1^2 E_{ii}$, using the extended and interpolated data are presented in Fig. 14, in both linear and logarithmic scales. Similar plots using the true spatial distributions are presented in Fig. 9. In both cases the plots of $k_1^2 E_{33}$ exhibit clear peaks at $k_1 \approx 100$–200 rad m^{-1}, suggesting that the wavelength of peak dis-

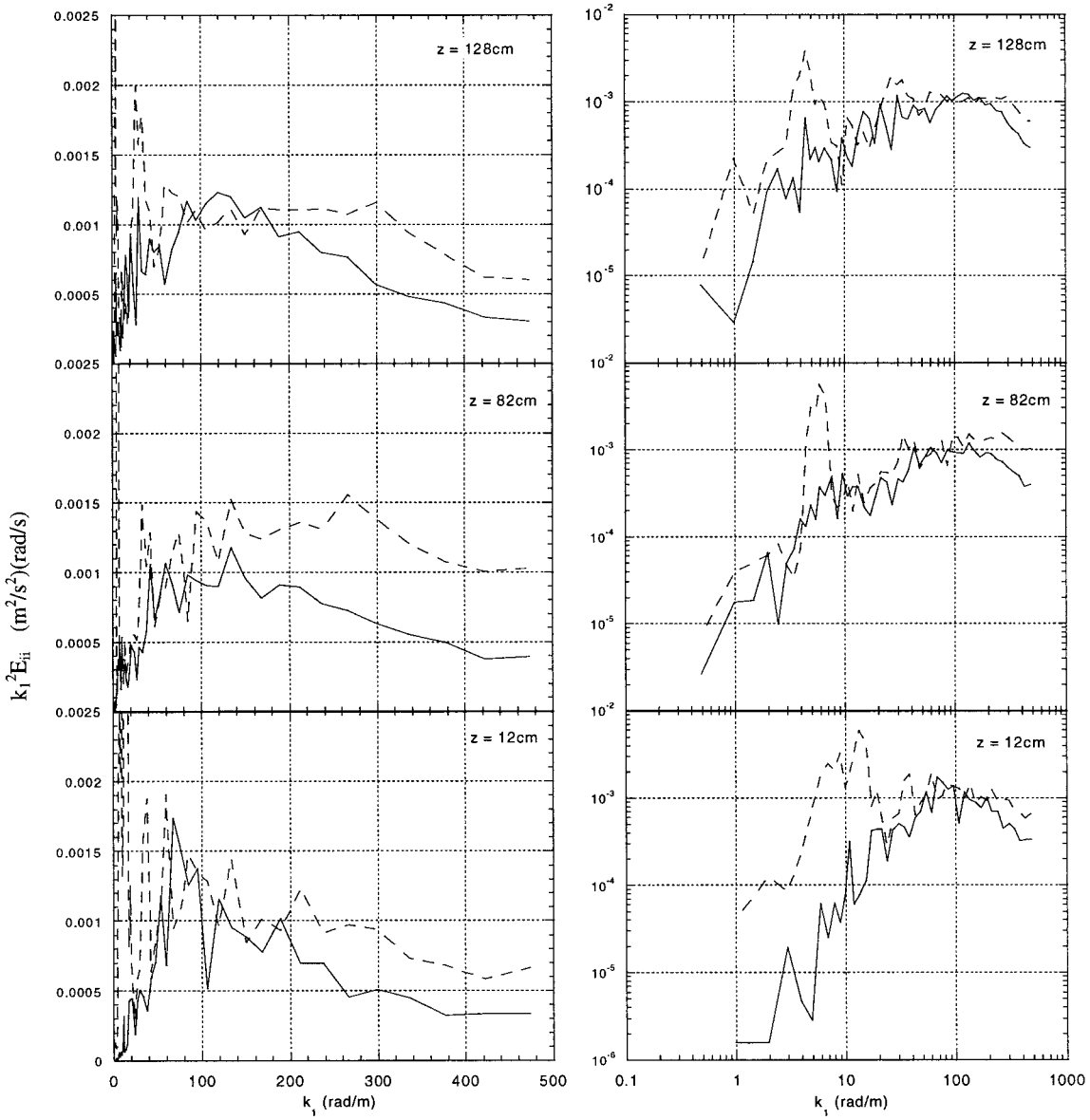

FIG. 14. Sample spectra of turbulent kinetic energy dissipation, calculated from the extended and interplotated vector maps. The logarithmic plots are shown to emphasize the spectral peaks. Solid lines: $k_1^2E_{33}$; dashed lines: $k_1^2E_{11}$.

sipation is 4–6 cm. Thus, the present data extends to wavenumbers well in the dissipation range. In this section we use the PIV data to compare several methods for estimating the dissipation rate, ε. Three of these methods are only possible with 2D spatial velocity distributions and the other two are based on the energy and dissipation spectra. Each method is summarized below.

a. ''Direct'' estimate of the dissipation

For a Newtonian fluid the dissipation rate is defined as

$$\varepsilon = 2\nu S_{ij}S_{ij} = \nu\frac{\partial u_i}{\partial x_j}\left(\frac{\partial u_i}{\partial x_j} + \frac{\partial u_j}{\partial x_i}\right), \tag{8}$$

where ν is the kinematic viscosity and double indices indicate summation over all three directions. Using planar PIV we can measure the following five of the terms in Eq. (8) directly:

$$\left(\frac{\partial u}{\partial x}\right)^2, \quad \left(\frac{\partial w}{\partial z}\right)^2, \quad \left(\frac{\partial u}{\partial z}\right)^2, \quad \left(\frac{\partial w}{\partial x}\right)^2, \quad \left(\frac{\partial u}{\partial z}\frac{\partial w}{\partial x}\right). \tag{9}$$

Using continuity we obtain

$$\left(\frac{\partial v}{\partial y}\right)^2 = \left(-\frac{\partial u}{\partial x} - \frac{\partial w}{\partial z}\right)^2$$

$$= \left(\frac{\partial u}{\partial x}\right)^2 + \left(\frac{\partial w}{\partial z}\right)^2 + 2\left(\frac{\partial u}{\partial x}\frac{\partial w}{\partial z}\right). \quad (10)$$

For isotropic turbulence, the terms in Eqs. (9) and (10) constitute 8/15 of the total dissipation. Additional terms are estimated, assuming that all lateral fluctuations have similar average magnitudes:

$$\left(\frac{\partial u}{\partial y}\right)^2 = \left(\frac{\partial w}{\partial y}\right)^2 = \left(\frac{\partial v}{\partial x}\right)^2 = \left(\frac{\partial v}{\partial z}\right)^2 = \frac{1}{2}\left[\left(\frac{\partial u}{\partial z}\right)^2 + \left(\frac{\partial w}{\partial x}\right)^2\right]$$

$$\left(\frac{\partial u}{\partial y}\frac{\partial v}{\partial x}\right) = \left(\frac{\partial w}{\partial y}\frac{\partial v}{\partial z}\right) = \left(\frac{\partial u}{\partial z}\frac{\partial w}{\partial x}\right). \quad (11)$$

Introducing into Eq. (12), we obtain a ''direct'' estimate of the dissipation rate, ε_D:

$$\varepsilon_D = 3\nu\left[\left\langle\left(\frac{\partial u}{\partial x}\right)^2\right\rangle + \left\langle\left(\frac{\partial w}{\partial z}\right)^2\right\rangle + \left\langle\left(\frac{\partial u}{\partial z}\right)^2\right\rangle + \left\langle\left(\frac{\partial w}{\partial x}\right)^2\right\rangle + 2\left\langle\left(\frac{\partial u}{\partial z}\frac{\partial w}{\partial x}\right)\right\rangle + \frac{2}{3}\left\langle\left(\frac{\partial u}{\partial x}\frac{\partial w}{\partial z}\right)\right\rangle\right]. \quad (12)$$

In this case, the only assumption is that the cross-stream gradients have the same average magnitude as the measured in-plane cross gradients. This assumption is supported by the similar magnitudes of the measured gradients, $(\partial u/\partial z)^2$ and $(\partial w/\partial x)^2$. In isotropic turbulence these assumptions become identities. In addition, all the directly measured gradients are used in the estimates. Thus, the assumptions leading to Eq. (12) are weaker than those involved in isotropy-based methods described in the following two sections. A similar approach for analyzing PIV data is employed by Fincham et al. (1996) using laboratory data.

b. Line fit in the inertial range

Using an assumption of isotropic homogeneous turbulence, at least in the inertial range (which is not accurate for the present data), the dissipation rate can be estimated from (Hinze 1975; Tennekes and Lumley 1972)

$$E_{11}(k_1) = \frac{18}{55}(1.6)\varepsilon_{\mathrm{LF}}^{2/3}k_1^{-5/3}. \quad (13)$$

The streamwise velocity spectra are more susceptible to contamination by surface waves (see section 7), which can leak to wavenumbers within the inertial range. Therefore, we evaluate the dissipation rate, $\varepsilon_{\mathrm{LF}}$, based on the isotropic ratio of $E_{11} = \frac{3}{4}E_{33}$ and use the values of A_{33} presented in Table 3. Similar estimates of $\varepsilon_{\mathrm{LF}}$ are obtained by fitting the Nasmyth universal spectrum (Oakey 1982) in the inertial range only. The method is essentially similar to that proposed by Stewart and Grant (1962) and has also been used extensively for estimating the dissipation rate in turbulent laboratory flows. We present results computed using both the extended and interpolated spectra and the true spatial spectra.

c. Integral of the dissipation spectrum

For homogeneous isotropic turbulence, the dissipation rate is

$$\varepsilon = 15\nu\left(\frac{\partial u}{\partial x}\right)^2 = \frac{15}{2}\nu\left(\frac{\partial w}{\partial x}\right)^2. \quad (14)$$

The Fourier representation of (14) can be used to estimate the dissipation rate from the one-dimensional spectrum of vertical velocity fluctuations (Monin and Yaglom 1975):

$$\varepsilon_{\mathrm{DS}} = \frac{15}{2}\nu\int_0^\infty k_1^2 E_{33}(k_1)\, dk_1. \quad (15)$$

The present data does not extend to the Kolmogorov scale. Moreover, at the largest wavenumbers there are indications of noise contamination in the dissipation spectra. Therefore, the area under the measured dissipation spectra represents only part of the total dissipation. To estimate the portion of ε in the range of k_1 that we do integrate, we use the Nasmyth universal spectrum. We first determine a cutoff wavenumber that constitutes the upper limit of the integral. This cutoff should be large enough to avoid loss of data and small enough to exclude noise. The universal spectrum is fitted to the measured data, such that the integrals of the universal spectrum and of the measured data are equal in the prescribed wavenumber range. Results of such fittings to the extended spectra are compared to the experimental data in Fig. 15. Then, since the total dissipation rate parameterizes the universal spectrum, the fitted Nasmyth spectrum provides a direct estimate for $\varepsilon_{\mathrm{DS}}$. In effect, $\varepsilon_{\mathrm{DS}}$ is evaluated by extending the measured fraction of the dissipation spectrum integral using the universal spectrum. This type of analysis is performed using both the true spatial spectra and the extended spectra.

For the present extended data, dissipation estimates obtained for two cutoff wavenumbers, $k_1 = 300$ and 470 rad m^{-1}, yield similar values that are within 10% of each other. The only exception is the data at the bottom station, where the difference is about 30%. This larger discrepancy can be attributed to the increasing impact of wave-induced motion in the wavenumber range containing the dissipation peak (only in the extended spectra). To explain this trend note that the location of wave-induced peaks in the extended spectra is shifted to a higher wavenumber with decreasing local convection velocity (the wavenumber is the frequency divided by the convection velocity). This problem not only moves the wave-induced spectral peak closer to the peak dissipation wavenumber, but also increases the contribution of wave contamination since dissipation scales with k_1^2. A lower cutoff increases the relative weight of this

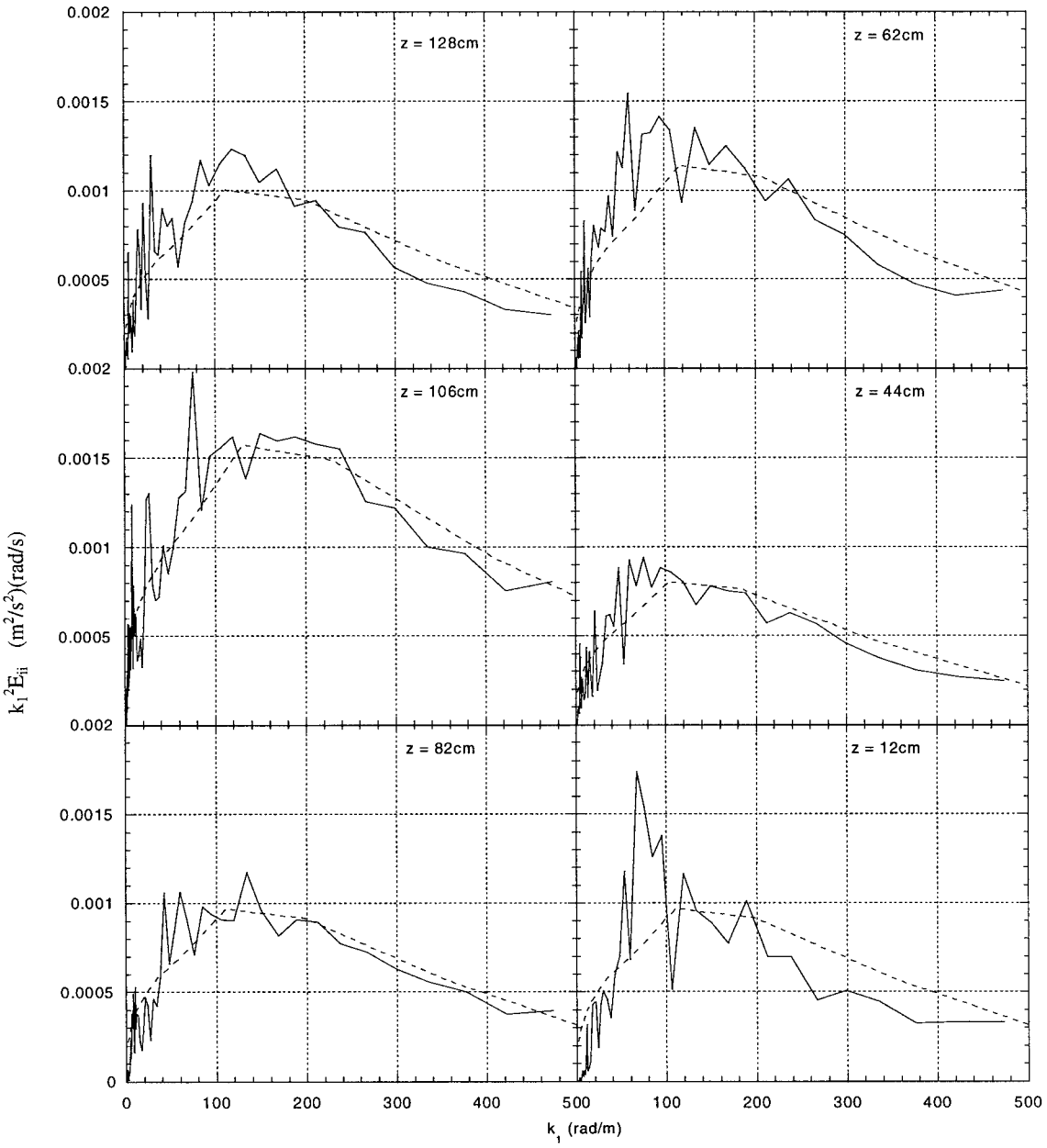

FIG. 15. Dissipation spectra based on the vertical velocity component ($k_1^2 E_{33}$). Solid lines: present data; dashed lines: Nasmyth universal spectrum.

contamination. On the other hand, high cutoffs may introduce noisy wavenumbers into the estimate. The values shown in Table 4 are calculated with the cutoff at $k_I = 300$ rad m^{-1}. Such problems emphasize the need to increase the sample area to a level that would allow measurements of spatial spectra over a range of scales that cover the entire domain affected by surface waves.

d. Locally axisymmetric turbulence

Considerable experimental data indicates that assumptions of local isotropy do not hold in a variety of flow situations. An alternative approach (e.g., George and Hussein 1991; Antonia et al. 1991) hypothesizes that the turbulence is locally axisymmetric, namely, invariant to rotations around a preferred axis (the streamwise direction in the present case). This assumption is less stringent than the requirements for isotropy, and leads to the following relationships:

$$\left(\frac{\partial u}{\partial y}\right)^2 = \left(\frac{\partial u}{\partial z}\right)^2; \qquad \left(\frac{\partial v}{\partial x}\right)^2 = \left(\frac{\partial w}{\partial x}\right)^2;$$

$$\left(\frac{\partial v}{\partial z}\right)^2 = \left(\frac{\partial w}{\partial y}\right)^2 \qquad \left(\frac{\partial v}{\partial y}\right)^2 = \frac{1}{3}\left[\left(\frac{\partial u}{\partial x}\right)^2 + \left(\frac{\partial v}{\partial z}\right)^2\right]$$

TABLE 4. Estimates of kinetic energy dissipation rates using the methods discussed in section 6a–e.

Elevation (cm)	"Direct" $\varepsilon_D \times 10^6$ (m^2 s^3)	"Direct" η (mm)	$\varepsilon_{LF} \times 10^6$ (m^2 s^3) line fit: Extended	$\varepsilon_{LF} \times 10^6$ (m^2 s^3) line fit: True spatial	$\varepsilon_{DS} \times 10^6$ (m^2 s^3) dissipation spectra: Extended	$\varepsilon_{DS} \times 10^6$ (m^2 s^3) dissipation spectra: True spatial	$\varepsilon_{AS} \times 10^6$ (m^2 s^3)	$\varepsilon_{SG} \times 10^6$ (m^2 s^3)
128	3.9	0.92	5.8	5.6	74.3	6.1	3.7	4.8
106	6.0	0.82	8.8	10.7	8.2	10.9	5.3	10.5
82	3.3	0.95	5.2	4.5	4.1	5.3	3.0	3.6
62	4.1	0.90	7.3	6.1	5.7	6.6	3.7	5.8
44	3.1	0.97	3.7	4.4	3.2	5.3	2.8	2.8
12	4.1	0.90	4.5	6.2	4.1	9.1	3.9	7.9

$$\frac{\partial v}{\partial z}\frac{dw}{dv} = \frac{1}{6}\left[\left(\frac{\partial u}{\partial x}\right)^2 - 2\left(\frac{\partial v}{\partial z}\right)^2\right]$$

$$\left(\frac{\partial u}{\partial y}\frac{\partial v}{\partial x}\right) = \left(\frac{\partial u}{\partial z}\frac{\partial w}{\partial x}\right) = -\frac{1}{2}\left(\frac{\partial u}{\partial x}\right)^2. \quad (16)$$

The dissipation rate can then be estimated from gradients in the measurement plane:

$$\varepsilon_{AS} = \nu\left[-\left(\frac{\partial u}{\partial x}\right)^2 + 8\left(\frac{\partial w}{\partial z}\right)^2 + 2\left(\frac{\partial u}{\partial z}\right)^2 + 2\left(\frac{\partial w}{\partial x}\right)^2\right]. \quad (17)$$

e. Energy flux across equilibrium range

Large eddy simulation of turbulent flows is based on filtered Navier–Stokes equations (e.g., Rogallo and Moin 1984; Lesieur and Metais 1996):

$$\frac{\partial \tilde{u}_i}{\partial t} + \tilde{u}_j\frac{\partial \tilde{u}_i}{\partial x_j} = -\frac{\partial}{\partial x_j}\left(\frac{\tilde{p}}{\rho}\delta_{ij} + \tau_{ij}\right) + \nu\frac{\partial^2 \tilde{u}_i}{\partial x_j \partial x_j}, \quad (18)$$

where the tilde denotes a spatial filtering operation at a scale Δ, and the subgrid-scale stress tensor is defined as

$$\tau_{ij} = \widetilde{u_i u_j} - \tilde{u}_i\tilde{u}_j. \quad (19)$$

If the scale of the filter corresponds to wavelengths within the inertial range, the condition of equilibrium suggests that the energy flux to smaller (subgrid) scales should provide an estimate of the dissipation rate (Liu et al. 1994, 1999). Thus,

$$\varepsilon_{SG} = -\tau_{ij}\tilde{S}_{ij}, \quad (20)$$

where $\tilde{S}_{ij} = \frac{1}{2}(\partial\tilde{u}_i/\partial x_j + \partial\tilde{u}_j/\partial x_i)$ is the filtered strain-rate tensor. Since planar PIV provides only part of the tensor terms, we approximate the others, similar to the approach utilized in section 6a. Inserting the known and approximated terms,

$$\tau_{12}\tilde{S}_{12} = \tau_{23}\tilde{S}_{23} = \tau_{13}\tilde{S}_{13}$$

$$\tau_{22}\tilde{S}_{22} = \frac{1}{2}(\tau_{11}\tilde{S}_{11} + \tau_{33}\tilde{S}_{33}), \quad (21)$$

into Eq. (24) yields the subgrid-scale energy flux estimate of the dissipation rate:

$$\varepsilon_{SG} = \frac{1}{2}(3\tau_{11}\tilde{S}_{11} + 3\tau_{33}\tilde{S}_{33} + 12\tau_{13}\tilde{S}_{13}). \quad (22)$$

Note that this estimate is based on a third-order moment of the velocity, while all the previous methods are based on second-order moments. Also, since the dissipation rate is calculated from filtered strain rates and the stresses are typically dominated by the largest subgrid scales, substantial fraction of the high wavenumber noise is removed.

We need to ensure that the spatial filtering is done at a scale within the inertial range. At the same time, we need to minimize this scale in order to have as many data points on the filtered grid as possible. We set the filter size Δ to eight vector spacings (corresponding to a wavenumber of $k_1 = 124$ rad m^{-1}). While this value may be somewhat too low, it is the largest one that allows us to have a filtered array of 3×3 vectors from each instantaneous vector map. The local filtered strain rates are evaluated by offsetting the filtered grids by one vector spacing and finding the difference between offset filtered velocities.

f. Results and discussion in dissipation estimates

The kinetic energy dissipation rate estimates obtained by the various methods are presented in Table 4 and Fig. 16. For ε_{LF} and ε_{DS}, Table 4 presents results calculated using both the extended/interpolated and the averaged true spatial spectra. Also included are the values of the Kolmogorov length scale, η, using the "direct" dissipation rate; that is,

$$\eta = \left(\frac{\nu^3}{\varepsilon_D}\right)^{1/4}. \quad (23)$$

The kinematic viscosity of seawater at the measured temperature of the test site (9°C) is $\nu = 1.4 \times 10^{-6}$ m^2 s^{-1} (Kennish 1989). All the methods provide the same order-of-magnitude estimates for the dissipation rates. The largest discrepancies occur at the lowest elevation where the maximum difference, 3.9×10^{-6} versus 9.1×10^{-6}, is between ε_{AS} and ε_{DG} (TS data). Most of the discrepancies, however, are considerably smaller. The present dissipation rate estimates are within the range of typical values. For example, they are comparable to

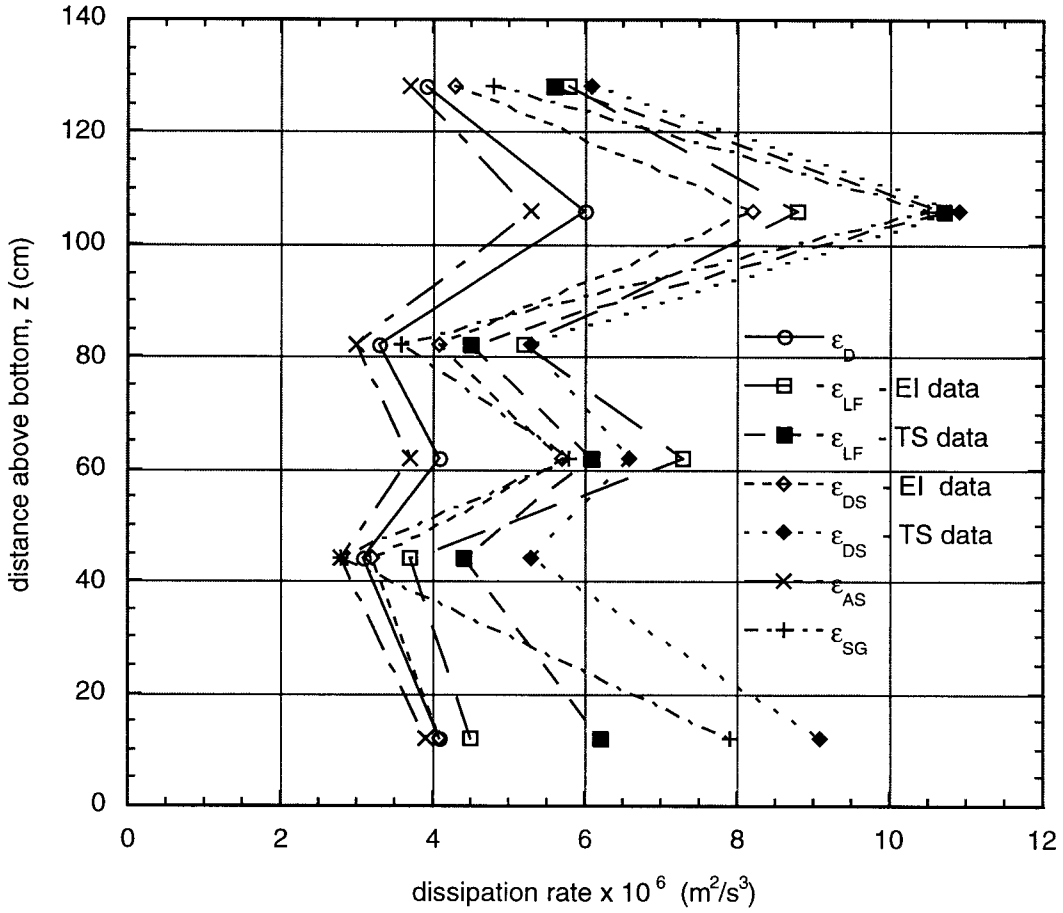

FIG. 16. Estimates of dissipation rate at the six measurement stations, obtained using different estimation methods. Note that this figure represents both spatial and temporal variations due to the 15-min time delay between successive stations.

values reported by Simpson et al. (1996) for a well-mixed boundary layer in the Irish Sea, by Gross et al. (1994) for off the California coast, and also to the data of Gargett et al. (1984). However, the present values of ε are somewhat larger than some values obtained in coastal waters (e.g., Stewart and Grant 1962; Oakey 1982; Dewey and Crawford 1988; Gargett 1994; Lueck et al. 1997), but are smaller than values measured in a tidal bottom boundary layer (Sanford and Lien 1999), in a tidal channel (Gargett and Moum 1995), and over a rippled bed (Agrawal and Aubrey 1992).

The most straightforward dissipation rate estimate is provided by the ''direct'' method (ε_D). As expected, the locally axisymmetric turbulence dissipation estimates, ε_{AS}, are very close to ε_D, with differences varying between 5% and 11% (ε_{AS} is systematically smaller). Estimation of dissipation using a third-order moment (ε_{SG}) requires a large number of data points to converge. For example, more than 40 000 points are required for convergence in the jet data of Liu et al. (1994). In the present case we only have a total of 1170 points, which affects the statistical confidence. Therefore, the ε_{SG} values show the largest fluctuations in trend relative to the other estimates.

The line-fit and dissipation-integral methods, ε_{LF} and ε_{DS}, respectively, determined either from the extended or from the true spatial spectra, yield results that are generally higher than ε_D. This trend agrees with the results of Fincham et al. (1996), who find that the assumption of isotropy leads to an overprediction of the dissipation rate by as much as 375% for stratified grid turbulence. In our case the characteristic differences are smaller and, except for one case (ε_{DS} using the TS spectra at the lowest elevation), they are significantly less than 100%. Using the extended and interpolated data, the estimates from the integral of the dissipation spectra (ε_{DS}) are closer to ε_D, probably since they are based on the whole range of available data, whereas the ($-5/3$) line-fit estimates are only based on a portion of the available spectrum. Also, the relative effect of contamination by wave-induced motion is probably larger for ε_{LF} since it is based on a range of wavenumbers that is closer to the equivalent scale of the waves (see section 7). Even though the dissipation is also contaminated by

the waves, the major contribution to its value comes from much smaller scales.

The line-fit dissipation estimates obtained from the true spatial spectra are typically within 20% of the estimates based on the extended data. Only at the lowest station, at $z = 12$ cm, is the discrepancy considerably larger (37%). At this elevation the wavenumber range with a $-5/3$ slope is quite small, and the accuracy of the slope-based estimates is low. Consistent with the comparisons shown in Fig. 12, the dissipation estimates based on integrating the true spatial dissipation spectra are 29%–122% higher than the corresponding estimates based on the interpolated data. Once again, the largest discrepancy is near the bottom. All the dissipation estimates using TS data yield larger values than the corresponding values of ε_D.

It is reassuring that despite the numerous assumptions involved in some of the estimation methods, all of them reproduce the trends of the dissipation rates at the various stations. Note that the profile shown in Fig. 16 actually represents both spatial and temporal variations due to the time delay between measurements. The vertical distribution of dissipation rate is nearly uniform (within 33% for each of the methods) at all elevations, except for $z = 106$ cm where it is significantly higher, irrespective of the method used for estimating ε. At this station, the dissipation is nearly twice as large. As noted before, this data series was the last one to be recorded and it occurred after a tidal change. At this elevation both the mean velocity (Fig. 4) and turbulence level (Fig. 9) reach maximum levels.

7. Effects of wave–turbulence interaction

In this section we address the effect of waves on the turbulence spectra. The surface waves induce unsteady velocity components at temporal scales that are comparable to the characteristic turbulence timescales, although the spatial scales of the waves are much larger than those of the turbulence. The unsteady pressure, which is mostly a result of surface waves, is recorded simultaneously with the PIV data, at a rate of 7 Hz. The frequency-domain power spectrum of the pressure is computed using FFT and then translated to ''equivalent wavenumbers'' using the mean convection velocity at each elevation; that is, $k = 2\pi f_w/U$, where f_w is the frequency of the wave.

Figure 17 shows three sample pressure spectra together with the EI velocity spectra. It is evident that there are several surface wave peaks that coincide with energy peaks. The highest peak in the pressure spectrum, which exists in all the data (including results not shown here), appears to have a period of about 7.5 s. Since the convection velocity increases with elevation, the spectral peaks are shifted to lower wavenumbers with increasing elevation. At $z = 12$ cm the peak is at $k_1 = 10.3$ rad m^{-1}, whereas at $z = 1.2$ m the peak is at $k_1 = 3.9$ rad m^{-1}. Some of the peaks of the pressure

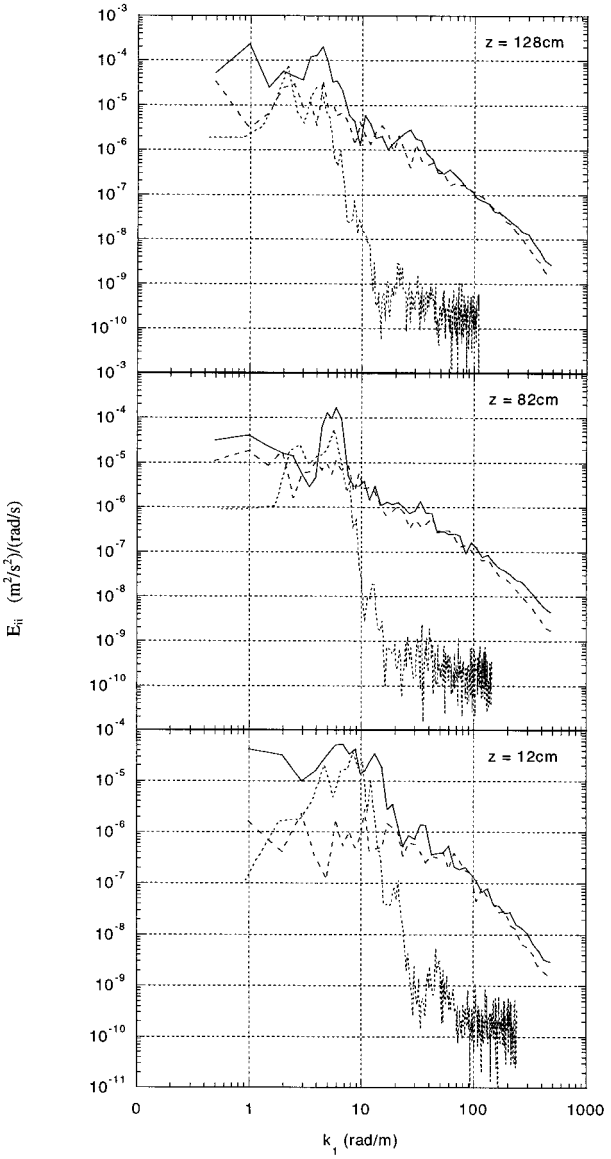

FIG. 17. Sample spectra of pressure signal (converted to equivalent wavenumbers) and velocity. Solid lines: E_{11}, dashed lines: E_{33}, dotted lines: pressure (in arbitrary units).

spectra coincide with peaks in the horizontal velocity spectra. This agreement indicates that the shape of the velocity spectra in that range is affected significantly by the wave motion, in addition to the large-scale turbulence.

According to linear wave theory (Dean and Dalrymple 1984),

$$u_w = \eta_w \sigma \frac{\cosh k_w(h + \zeta)}{\cosh k_w h} \tag{24}$$

$$w_w = \eta_w \sigma \tan\sigma t \frac{\sinh k_w(h + \zeta)}{\sinh k_w h}, \tag{25}$$

where u_w and w_w are the horizontal and vertical wave-

induced velocities, respectively, h is the mean depth, ζ is the distance below the mean surface ($\zeta = 0$ at the surface, $\zeta = -h$ at the bottom), η_W is the surface displacement given by $\eta_W = \eta_0 \cos(k_W x - \sigma t)$, and the angular frequency σ is given by the dispersion relation $\sigma = Uk_W + \sqrt{gk_W \tanh k_w h}$. Equations (24) and (25) indicate that the wave frequency affects the amplitude of the induced velocity. Thus, two pressure peaks with the same magnitude but at different k_W, and therefore different σ, will have a different effect on the velocity. For example, at $z = 128$ cm (Fig. 17) the u spectral peak associated with the pressure at $k_1 = 2.1$ rad m^{-1} is lower than the corresponding peak at $k_1 = 4.2$ rad m^{-1}, although the relative magnitude of the pressure peaks is the opposite. Note, however, that this trend may also be caused by a wave propagating out of plane, at an angle to the x axis of our vector maps. Such a wave would have a reduced effect on the measured horizontal velocity, whereas the pressure spectrum would not be affected by the wave direction.

The wave effect on the vertical velocity depends on $\sinh k_W(h + z)$ and is therefore significantly weaker, especially near the bottom ($z \to -h$), as demonstrated in all the spectra of the vertical velocity and also in the distributions shown in Fig. 6. Similar trends for both u and w are reported by Agrawal and Aubrey (1992). Consequently, in the past researchers (Grant et al. 1984; Dewey and Crawford 1988; Huntley and Hazen 1988; Agrawal et al. 1992; Gargett 1994; Gross et al. 1994) have used the vertical velocity spectra to calculate the turbulence parameters. The expected increase in wave contamination of the w spectra with increasing distance from the bottom is also evident in Fig. 17.

In the data analysis presented in this paper we do not attempt to separate wave-induced unsteadiness and turbulence. The procedure proposed by Trowbridge (1998) to remove the wave contamination from the turbulence data cannot be applied to the present data since it requires data from points separated by more than the characteristic turbulence length scale. The present data provides measured velocities at locations separated by no more than 20 cm, which does not satisfy this requirement. To resolve this problem, in a recent deployment, we have recorded data that enables us to measure the true spatial spectra directly using structure functions up to a scale of 1.5 m ($k = 4.2$ rad m^{-1}). The data was obtained using two cameras simultaneously, each with a sample area of 50 cm $\times$ 50 cm, that are located 1 m apart. In a sense, such use of two PIV images performs a similar function to the procedure proposed by Trowbridge (1998). However, in another sense this approach goes back to the original Kolmogorov structure functions.

We do not apply the pressure–velocity cross-correlation filtering method proposed by Agrawal and Aubrey (1992) since the present time series includes only 130 data points. Filtration of the wave effect will be attempted with longer data series, which will contain significantly more data points and thus can allow the velocity–pressure cross-correlation to converge. Rather than attempt a crude approach to isolating turbulence from wave-induced motion, we prefer to defer this analysis to datasets collected specifically to address this issue.

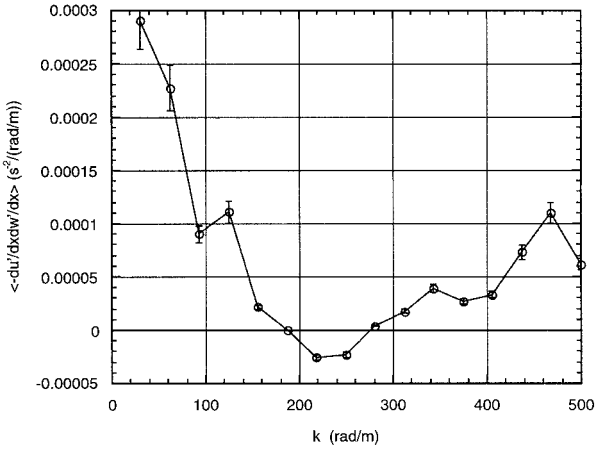

FIG. 18. True spatial shear cross-spectrum at $z = 20$ cm. The data is averaged over 130 vector maps and over three adjacent rows.

8. Velocity fluctuations and Reynolds stresses

''Contamination'' of the turbulence by the waves limits the usefulness of averaged parameters of velocity fluctuations that are based on the extended and interpolated data. The true spatial spectra are less affected but they are limited in length scales to the size of the vector map; that is, they contain only a small part of the turbulence spectrum unless the integral scale is comparable to the size of the vector map. Consequently, with the present system we can only obtain meaningful data on the turbulence parameters near the bottom where the integral scale of the vertical velocity component (but not the horizontal component) is comparable to the image size (see section 5d). Recognizing these limitations, one can still draw some interesting conclusions. For the lowest elevation we can use the true spatial shear cross-spectrum, that is, the spectrum of $u'_v w'_v$, to calculate the shear stress. Here u'_v and w'_v are the fluctuating velocity components with respect to the mean value for the same vector map and at the same elevation, that is,

$$u'_v = u(x_m, z) - \sum_{m=1}^{29} u(x_m, z);$$

$$w'_v = w(x_m, z) - \sum_{m=1}^{29} w(x_m, z). \qquad (26)$$

A sample cross-spectrum containing results averaged over three rows and 130 vector maps, for an elevation of 20 cm is presented in Fig. 18. As before, the error bars indicate a 95% confidence level. As is evident, we are still missing part of the shear spectrum in the low

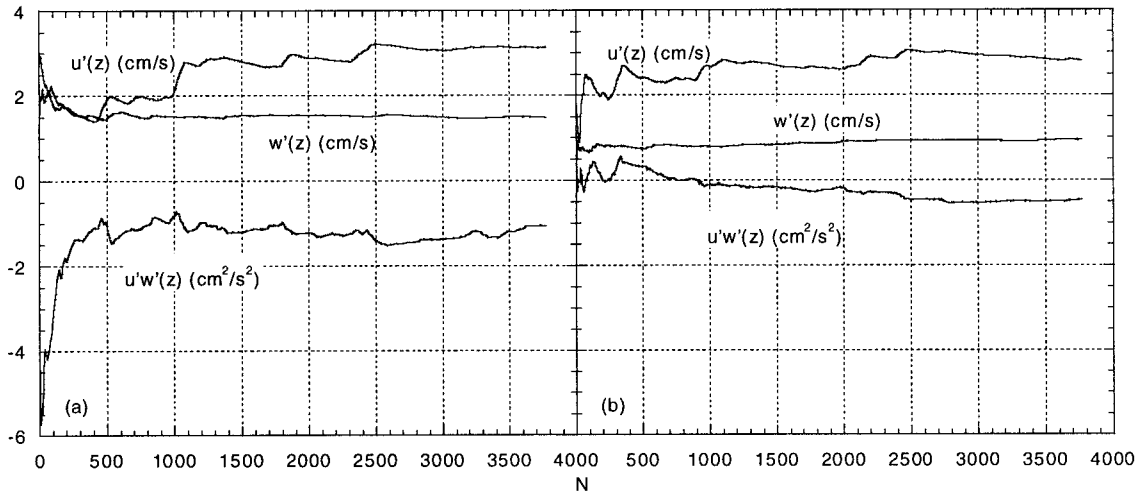

FIG. 19. Running rms averages of velocity fluctuations, $\sqrt{N^{-1}\,\Sigma_N\,(u'(z)^2)}$, $\sqrt{N^{-1}\,\Sigma_N\,(w'(z)^2)}$, and running average of $u'(z)w'(z)$, $N^{-1}\,\Sigma_N(u'(z)w'(z))$, as a function of number of points, N, used to compute the average. (a) $z = 128$ cm. (b) $z = 12$ cm.

wavenumber range and, as a result, integration within the available wavenumbers underpredicts the shear stress. Integration of the region $30 < k < 190$ rad m^{-1}, where the spectrum is positive, leads to $[\langle u'_v w'_v\rangle]^{1/2} = 3.4$ mm s^{-1}. The value of $[\langle w'^2_v\rangle]^{1/2}$ averaged over the same data is 7.3 mm s^{-1} (for simplicity we will omit the angle brackets and indicate the rms values as w'_v in subsequent equations). This value is calculated directly from the velocity distributions, without using the spectra. Thus, $|u'_v w'_v|/w'^2_v = 0.22$. This value is lower than the typical ratio of 0.3–0.4 measured in the outer region of turbulent boundary layers over smooth flat plates (Hinze 1975) with no pressure gradients. The difference may be attributed in part to the incomplete shear spectrum (but the w' spectrum is also incomplete) or to local positive pressure gradients that would decrease this ratio.

Unfortunately, the integral scale of u' is much larger than the vector map and, as a result, values of u'_v should be significantly smaller than the rms value of horizontal velocity fluctuations. In fact, for the high wavenumber range covered by the instantaneous data, the values of u'_v and w'_v are very close, as evidenced by the TS spectra. The differences between them occur mainly at lower wavenumbers, as the EI spectra show. Consequently, we cannot calculate the ratio $u'w'/q^2 = u'w'/0.5(u'^2 + v'^2 + w'^2)$ that is typically presented in the turbulence literature (typical value away from the boundary—0.16). Such a comparison would become possible once we obtain spectra free of wave contamination. Finally, note that assumptions based on isotropic turbulence lead to $w'_v = (\varepsilon l)^{1/3}$, where l is the integral length scale. Using the results in Table 4 and assuming $l = 20$ cm (the distance to the bottom), one finds $w'_v = 10$ mm s^{-1}, that is, of the same order as the measured values.

Before concluding, while keeping the wave contamination in mind, it is illuminating to present the overall measured velocity fluctuations. To calculate the distributions we assume horizontal homogeneity and define the rms velocity fluctuations relative to $U(z)$ and $W(z)$ as

$$u'(z) = \left(\frac{1}{130 \cdot 29}\sum_{n=1}^{130}\sum_{m=1}^{29}(u(x_m, z, t_n) - U(z))^2\right)^{1/2},$$

$$w'(z) = \left(\frac{1}{130 \cdot 29}\sum_{n=1}^{130}\sum_{m=1}^{29}(w(x_m, z, t_n) - W(z))^2\right)^{1/2}; \tag{27}$$

$U(z)$ and $W(z)$ are defined in Eqs. (1) and (2). To demonstrate the data convergence Fig. 19 contains sample running averages at two elevations. The vertical distributions of u' and w' are presented in Fig. 20, normalized

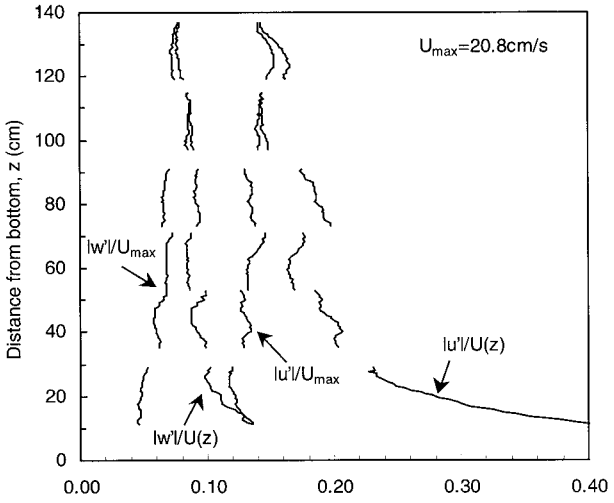

FIG. 20. Vertical profiles of rms velocity fluctuations [Eq. (26)]: $U(z)$ is the average horizontal velocity and U_{max} is the largest value of $U(z)$.

by both $U_{max} = U(z = 115 \text{ cm}) = 20.8 \text{ cm s}^{-1}$ (i.e., the maximum average velocity available from the present data), and $U(z)$, the local average velocity.

The magnitudes of the fluctuations are higher than those measured in laboratory flows over flat plates (e.g., Hinze 1975), mostly due to the wave contamination. At the lowest elevation w' is noticeably lower with characteristic values of 1.0 cm s, that is, slightly higher than $w'_v = 0.73 \text{ cm s}^{-1}$. Both an incomplete wavenumber range for the TS data and weak wave contamination may be the causes for the difference. At higher elevation w' increases and, as Fig. 6 shows, it is strongly affected by waves. The values of u' are substantially higher and clearly contaminated by waves. Consequently, the trends in Fig. 20 do not agree with laboratory boundary layer flows over smooth flat plates. There, the decrease in turbulence intensities is expected only at $z/\delta < 0.2$ for w' and $z/\delta < 0.01$ for u' (Hinze 1975). Bottom roughness also contributes to the increase in magnitude of velocity fluctuations (e.g., Krogstad et al. 1992; Shafi and Antonia 1997). Calculating the shear stresses assuming horizontal homogeneity leads to values that are significantly higher, 50 $\text{mm}^2 \text{ s}^{-2}$ at the lowest elevation, that is, 4.3 times higher than $u'_v w'_v$. These results are clearly dominated by wave effects. At higher elevations the values are doubled. The ratio $-u'w'/0.75(u'^2 + w'^2)$, which is an approximation for $-u'w'/q^2$, assuming $v'^2 = 0.5(u'^2 + w'^2)$, has values of 0.07 at the lowest elevation and ranges between 0.10 and 0.15 at the higher elevations. According to Hinze (1975), the characteristic value of $-u'w'/q^2$ in low Reynolds number, flat-plate boundary layers is about 0.16, vanishing at both edges. A lower ratio is expected in flows with positive pressure gradient (Townsend 1976). Saddoughi and Veeravalli (1994) measured values slightly smaller than 0.13, reducing to less than 0.10 near the wall and the outer edge, in a high–Reynolds number boundary layer. The data of Sanford and Lien (1999), from a tidal bottom boundary layer, show similar trends, with values of 0.12–0.13. It seems that, in spite of the contamination, the ratio is maintained in the present data.

9. Concluding remarks

Particle image velocimetry (PIV) provides two-dimensional velocity distributions within a prescribed sample area. While the technique is well established in laboratory studies, the present apparatus constitutes, to the best of our knowledge, the first implementation in an oceanic environment. Various tests, and in particular the latest deployment of the system in the New York Bight, have proved its feasibility and its ability to provide high quality data.

The two-dimensional velocity distributions obtained using PIV enable evaluation of turbulence spectra, which are based on true spatial distributions. The data also enables direct measurements of spatial velocity gradients, and consequently we can test some of the commonly used assumptions regarding the flow structure. In particular, in this paper we evaluate the accuracy of dissipation rate estimates obtained from spatial spectra that rely on assumptions of isotropy, Taylor's hypothesis, and the existence of an equilibrium inertial range. We also use the Taylor hypothesis to ''patch'' datasets together in order to extend the spectral range beyond the scale of an individual velocity distribution. Unfortunately, in doing so we also introduce wave contamination that does not exist in the true spatial spectra. Consequently, in recent experiments we have recorded instantaneous data with a sufficiently large range of scales (using multiple cameras) that will provide true spatial data for the entire domain susceptible to wave contamination.

While the large-scale turbulence in a boundary layer is necessarily anisotropic, it is common to regard the small-scale turbulence as locally isotropic and employ various forms of the Kolmogorov model. The present data clearly show departures from isotropy at all scales, including the viscous dissipation range. Furthermore, clear systematic differences exist between spectra of velocity components that are parallel and those that are perpendicular to the direction of the wavenumber. At five of the six elevations, the dissipation spectra of the perpendicular velocity components have peaks at $100 < k_i < 250$. Although one may detect traces of a local maximum at the same wavenumber range in the parallel velocity spectra, the dominant peaks are located in the $250 < k_i < 350$ range.

In comparing the present trends to previously published data, there is evidence that local isotropy may be approached away from walls (e.g., Gargett et al. 1984), but it is not observed close to boundaries (Antonia et al. 1991). In fact, Durbin and Speziale (1991) show that exact local isotropy cannot exist in the presence of mean shear. Anisotropy at the dissipation and inertial scales is demonstrated experimentally by Garg and Warhaft (1998) for a homogeneous shear flow in a wind tunnel. Saddoughi and Veeravalli (1994), for high Reynolds number flow, and Antonia and Kim (1994), for low Reynolds number flow, present criteria for a maximum strain rate that allows viewing the local turbulence as nearly isotropic. The magnitudes of the strain rate in the present data are near this limit or slightly above it. The dynamics of the small scales can also be affected by nonlocal interactions, where large-scale anisotropy directly affects the smallest scales (Brasseur and Wei 1994; Zhou et al. 1996). This effect becomes more significant as the scale separation increases. Thus, it is not surprising that the present data does not fulfill requirements for isotropy even at dissipation scales.

The integral length scale associated with the vertical velocity fluctuations (but not the horizontal velocity fluctuations) should scale with distance from the bottom, a trend that is clearly demonstrated in the present data. Consequently, the anisotropy at large scales increases as the bottom is approached. However, differences clear-

ly exist even at the highest elevation, 128 cm above the bottom.

In spite of the measured departure from the simplifying assumptions of homogeneity and isotropy, some general trends derived from these assumptions are supported by the present data. For example, dissipation rate estimates obtained using curve fits in the inertial range, integration of the dissipation spectrum and subgrid energy flux are 30%–100% higher than ''direct'' measurements that are based on the terms that can be obtained with the 2D data.

Acknowledgments. This project was funded by the ONR, Dr. L. Goodman, Project Manager, under Grant N00014-95-1-0215. Some of the instrumentation was purchased with DARPA funding.

The authors would like to thank G. Roth for developing the image-analysis codes and for his work on building the image acquisition system; S. King of Kingdom Electronics, Inc. for his invaluable work on the design and construction of the electronic systems and for his assistance in the field; K. Russell for his design of many of the mechanical components; Y. Ronzhes for mechanical design and for his assistance during the deployment; C. Meneveau for helpful discussions; S. McDowell and R. Valente of SAIC for their assistance in selecting the test site; and W. Corso, J. Hughes, and E. Reskow of the New Jersey Marine Sciences Consortium for their highly skilled support and flexibility during the deployment.

REFERENCES

Adrian, R. J., 1991: Particle-imaging techniques for experimental fluid mechanics. *Annu. Rev. Fluid Mech.,* **23,** 261–304.

Agrawal, Y., 1996: Laser sensors for high-resolution velocity and dissipation measurements. *Proc. Workshop on Microstructure Sensors in the Ocean*, Mt. Hood, OR, Office of Naval Research, 15–23.

——, and D. G. Aubrey, 1992: Velocity observations above a rippled bed using Laser Doppler Velocimetry. *J. Geophys. Res.,* **97** (C12), 20 249–20 259.

——, E. A. Terray, M. A. Donelan, P. A. Hwang, A. J. Williams, W. M. Drennan, K. K. Kahma, and S. A. Kitaigorodskii, 1992: Enhanced dissipation of kinetic energy beneath surface waves. *Nature*, **359,** 219–220.

Antonia, R. A., and J. Kim, 1994: A numerical study of local isotropy of turbulence. *Phys. Fluids,* **6,** 834–841.

——, ——, and L. W. B. Browne, 1991: Some characteristics of small-scale turbulence in a turbulent duct flow. *J. Fluid Mech.,* **233,** 369–388.

Bertuccioli, L., G. I. Roth, J. Katz, and T. R. Osborn, 1999: A submersible Particle Image Velocimetry system for turbulence measurements in the bottom boundary layer. *J. Atmos. Oceanic Technol.,* **16,** 1635–1646.

Brasseur, J. G., and C. H. Wei, 1994: Interscale dynamics and local isotropy in high Reynolds number turbulence within triadic interactions. *Phys. Fluids,* **6,** 842–870.

Dean, R. G., and R. A. Dalrymple, 1984: *Water Wave Mechanics for Engineers and Scientists.* Prentice-Hall, 353 pp.

Dewey, R. K., and W. R. Crawford, 1988: Bottom stress estimates from vertical dissipation rate profiles on the continental shelf. *J. Phys. Oceanogr.,* **18,** 1167–1177.

Dong, R., S. Chu, and J. Katz, 1992: Quantitative visualization of the flow within the volute of a centrifugal pump. Part A: Technique. *J. Fluids Eng.,* **114,** 390–395.

Durbin, P. A., and C. G. Speziale, 1991: Local anisotropy in strained turbulence at high Reynolds numbers. *J. Fluids Eng.,* **113,** 707–709.

Emery, W. J., and R. E. Thomson, 1997: *Data Analysis Methods in Physical Oceanography.* Pergamon, 634 pp.

Falkovich, G., 1994: Bottleneck phenomenon in developed turbulence. *Phys. Fluids,* **6,** 1411–1414.

Fincham, A. M., T. Maxworthy, and G. R. Spedding, 1996: Energy dissipation and vortex structure in freely decaying, stratified grid turbulence. *Dyn. Atmos. Oceans,* **23,** 155–169.

Garg, S., and Z. Warhaft, 1998: On the small-scale structure of simple shear flow. *Phys. Fluids,* **10,** 662–673.

Gargett, A. E., 1994: Observing turbulence with a modified acoustic Doppler current profiler. *J. Atmos. Oceanic Technol.,* **11,** 1592–1610.

——, and J. N. Moum, 1995: Mixing efficiencies in turbulent tidal fronts: Results from direct and indirect measurements of density flux. *J. Phys. Oceanogr.,* **25,** 2583–2608.

——, T. R. Osborn, and P. W. Nasmyth, 1984: Local isotropy and the decay of turbulence in a stratified fluid. *J. Fluid Mech.,* **144,** 231–280.

George, R., 1996: A review of acoustic Doppler velocimeter (ADV) tests and deployments. *Proc. Workshop on Microstructure Sensors in the Ocean*, Mt. Hood, OR, Office of Naval Research, 116–120.

——, and H. J. Hussein, 1991: Locally axisymmetric turbulence. *J. Fluid Mech.,* **233,** 1–23.

Grant, I., 1997: Particle image velocimetry: A review. *Proc. Inst. Mech. Eng., Part C*: *Mech. Eng. Sci.,* **211,** 55–76.

Grant, W. D., A. J. Williams, and S. M. Glenn, 1984: Bottom stress estimates and their prediction on the Northern California continental shelf during CODE-1: The importance of wave–current interaction. *J. Phys. Oceanogr.,* **14,** 506–527.

Gross, T. F., A. J. Williams, and E. A. Terray, 1994: Bottom boundary layer spectral dissipation estimates in the presence of wave motions. *Contin. Shelf Res.,* **14,** 1239–1256.

Hinze, J. O., 1975: *Turbulence.* 2d ed. McGraw-Hill, 790 pp.

Huntley, D. A., 1988: A modified inertial dissipation method for estimating seabed stresses at low Reynolds numbers, with application to wave/current boundary layer measurements. *J. Phys. Oceanogr.,* **18,** 339–346.

——, and D. G. Hazen, 1988: Seabed stresses in combined wave and steady flow conditions on the Nova Scotia continental shelf: Field measurements and predictions. *J. Phys. Oceanogr.,* **18,** 347–362.

Johnson, G. C., T. B. Sanford, and M. O. Baringer, 1994: Stress on the Mediterranean outflow plume. Part II: Turbulent dissipation and shear measurements. *J. Phys. Oceanogr.,* **24,** 2084–2092.

Keane, R. D., and R. J. Adrian, 1992: Theory of cross-correlation analysis of PIV images. *Appl. Sci. Res.,* **49,** 191–215.

Kennish, M., Ed., 1989: *CRC Practical Handbook of Marine Science.* CRC Press, 710 pp.

Kraus, N. C., A. Lohrmann, and R. Cabrera, 1994: New acoustic meter for measuring 3D laboratory flows. *J. Hydrol. Eng.,* **120,** 406–412.

Krogstad, P. A., R. A. Antonia, and L. W. B. Browne, 1992: Comparison between rough-wall and smooth-wall turbulent boundary-layers. *J. Fluid Mech.,* **245,** 599–617.

Lesieur, M., and O. Metais, 1996: New trends in large-eddy simulations of turbulence. *Annu. Rev. Fluid Mech.,* **28,** 45–82.

Lhermitte, R., and U. Lemmin, 1994: Open-channel flow and turbulence measurement by high-resolution Doppler sonar. *J. Atmos. Oceanic Technol.,* **11,** 1295–1308.

Liu, S., C. Meneveau, and J. Katz, 1994: On the properties of similarity subgrid-scale models as deduced from measurements in a turbulent jet. *J. Fluid Mech.,* **275,** 83–119.

——, J. Katz, and C. Meneveau, 1999: Evolution and modeling of

subgrid scales during rapid straining of turbulence. *J. Fluid Mech.,* **387,** 281–320.

Lohrmann, A., B. Hackett, and L. P. Roed, 1990: High-resolution measurements of turbulence, velocity and stress using a pulse-to-pulse coherent sonar. *J. Atmos. Oceanic Technol,* **7,** 19–37.

Lohse, D., and A. Muller-Groeling, 1995: Bottleneck effects in turbulence: Scaling phenomena in *r* versus *p* space. *Phys. Rev. Lett.,* **74,** 1747–1750.

Lu, Y., and R. G. Lueck, 1999: Using a broadband ADCP in a tidal channel. Part II: Turbulence. *J. Atmos. Oceanic Technol.,* **16,** 1568–1579.

Lueck, R. G., D. Huang, D. Newman, and J. Box, 1997: Turbulence measurement with a moored instrument. *J. Atmos. Oceanic Technol.,* **14,** 143–161.

Monin, A. S., and A. M. Yaglom, 1975: *Statistical Fluid Mechanics: Mechanics of Turbulence.* Vol. 2. The MIT Press, 874 pp.

Nautical Software, Inc., 1998: Tides and Currents. Version 2. Nautical Software, Inc.

Oakey, N. S., 1982: Determination of the rate of dissipation of turbulent energy from simultaneous temperature and velocity shear microstructure measurements. *J. Phys. Oceanogr.,* **12,** 256–271.

Rogallo, R. S., and P. Moin, 1984: Numerical simulation of turbulent flows. *Annu. Rev. Fluid Mech.,* **16,** 99–137.

Roth, G. I., D. Hart, and J. Katz, 1995: Feasibility of using the L64720 video motion estimation processor (MEP) to increase efficiency of velocity map generation for particle image velocimetry (PIV). *Proc. ASME, ASME Fluids Engineering Division Summer Meeting, Laser Anemometry* 1995, Hilton Head, SC, 387–394.

——, D. T. Mascenik, and J. Katz, 1999: Measurements of the flow structure and turbulence within a ship bow wave. *Phys. Fluids,* **11,** 3512–3523.

Saddoughi, S. G., and S. V. Veeravalli, 1994: Local isotropy in turbulent boundary layers at high Reynolds number. *J. Fluid Mech.,* **268,** 333–372.

SAIC, 1995: Results from the August 1995 Bathymetric survey of the expanded Mud Dump area. Science Applications International Corporation Tech. Rep. 353, submitted to U.S. Army Corps of Engineers—New York District, Contract No. DACW-51-95-D-0027.

——, 1996: Results from the October 1995 REMOTS survey of the expanded Mud Dump area. Science Applications International Corporation Tech. Rep. 364, submitted to U.S. Army Corps of Engineers—New York District, Contract No. DACW-51-95-D-0027.

Sanford, T. B., and R. C. Lien, 1999: Turbulent properties in a homogeneous tidal bottom boundary layer. *J. Geophys. Res.,* **104** (C1), 1245–1257.

——, J. A. Carlson, J. H. Dunlap, M. D. Prater, and R. C. Lien, 1999: An electromagnetic vorticity and velocity sensor for observing finescale kinetic fluctuations in the ocean. *J. Atmos. Oceanic Technol.,* **16,** 1647–1667.

Schwab, W. C., and Coauthors,1997: Initial results of high-resolution seafloor mapping offshore of the New York–New Jersey metropolitan area using sidescan sonar. *Northeast. Geol. Environ. Sci.,* **19,** 243–262.

Shafi, H. S., and R. A. Antonia, 1997: Small-scale characteristics of a turbulent boundary layer on a rough wall. *J. Fluid Mech.,* **342,** 263–293.

Simpson, J. H., W. R. Crawford, T. P. Rippeth, A. R. Campbell, and V. S. Cheok, 1996: The vertical structure of turbulent dissipation in shelf seas. *J. Phys. Oceanogr.,* **26,** 1579–1590.

Sridhar, G., and J. Katz, 1995: Drag and lift forces on microscopic bubbles entrained by a vortex. *Phys. Fluids,* **7,** 389–399.

——, and ——, 1999: Effect of entrained bubbles on the structure of vortex rings. *J. Fluid Mech.,* **204,** 171–202.

Stewart, R. W., and H. L. Grant, 1962: Determination of the rate of dissipation of turbulent energy near the sea surface in the presence of waves. *J. Geophys. Res.,* **67** (8), 3177–3180.

Tennekes, H., and J. L. Lumley, 1972: *A First Course in Turbulence.* The MIT Press, 300 pp.

Townsend, A. A., 1976: *The Structure of Turbulent Shear Flow.* 2d ed. Cambridge University Press, 429 pp.

Trowbridge, J. H., 1998: On a technique for measurement of turbulent shear stress in the presence of surface waves. *J. Atmos. Oceanic Technol.,* **15,** 290–298.

——, and Y. C. Agrawal, 1995: Glimpses of a wave boundary layer. *J. Geophys. Res.,* **100** (C10), 20 729–20 743.

——, A. J. Williams, and W. J. Shaw, 1996: Measurement of Reynolds stress and heat flux with an acoustic travel-time current meter. *Proc. Workshop on Microstructure Sensors in the Ocean,* Mt. Hood, OR, Office of Naval Research, 143–150.

van Haren, H., N. Oakey, and C. Garrett, 1994: Measurements of internal wave band eddy fluxes above a sloping bottom. *J. Mar. Res.,* **52,** 909–946.

Voulgaris, G., and J. H. Trowbridge, 1998: Evaluation of the acoustic Doppler velocimeter (ADV) for turbulence measurements. *J. Atmos. Oceanic Technol.,* **15,** 272–289.

Williams, A. J., J. S. Tochko, R. L. Koehler, T. F. Gross, W. D. Grand, and C. V. R. Dunn, 1987: Measurement of turbulence with an acoustic current meter array in the oceanic bottom boundary layer. *J. Atmos. Oceanic Technol.,* **4,** 312–327.

——, F. T. Thwaites, and A. T. Morrison, 1996: Transducer supports for acoustic travel-time current meters—Flow sampling, wake, and potential flow distortion considerations. *Proc. Workshop on Microstructure Sensors in the Ocean,* Mt. Hood, OR, Office of Naval Research, 38–43.

Winkel, D. P., M. C. Gregg, and T. B. Sanford, 1996: Resolving oceanic shear and velocity with the multi-scale profiler. *J. Atmos. Oceanic Technol.,* **13,** 1046–1072.

Zhou, Y., P. K. Yeung, and J. G. Brasseur, 1996: Scale disparity and spectral transfer in anisotropic numerical turbulence. *Phys. Rev. E,* **53,** 1261–1264.